# REAL-TIME STABILITY ANALYSIS IN FOOD SYSTEMS WITH MAGNETIC RESONANCE

A THESIS SUBMITTED TO
THE GRADUATE SCHOOL OF NATURAL AND APPLIED SCIENCES
OF
MIDDLE EAST TECHNICAL UNIVERSITY

BY

ERDEM MERCAN

IN PARTIAL FULFILLMENT OF THE REQUIREMENTS
FOR
THE DEGREE OF MASTER OF SCIENCE
IN
FOOD ENGINEERING

AUGUST 2024

Approval of the thesis:

**REAL-TIME STABILITY ANALYSIS IN FOOD SYSTEMS WITH MAGNETIC RESONANCE**

submitted by **ERDEM MERCAN** in partial fulfillment of the requirements for the degree of **Master of Science** i**n Food Engineering, Middle East Technical University** by,

Prof. Dr. Naci Emre Altun
Dean, **Graduate School of Natural and Applied Sciences** _____

Prof. Dr. Hami Alpas
Head of the Department, **Food Engineering** _____

Prof. Dr. Mecit Halil Öztop
Supervisor, **Food Engineering, METU** _____

Prof. Dr. Rob Morris
Co-Supervisor, **Physics, Nottingham Trent University** _____

**Examining Committee Members:**

Prof. Dr. Hami Alpas
Food Engineering Department, METU _____

Prof. Dr. Mecit H. Öztop
Food Engineering Department, METU _____

Prof. Dr. Rob Morris
Physics, Nottingham Trent University _____

Prof. Dr. Behiç Mert
Food Engineering Department, METU _____

Doç. Dr. Emin Burçin Özvural
Food Engineering, Çankırı Karatekin University _____

Date: 28.08.2024

**I hereby declare that all information in this document has been obtained and presented in accordance with academic rules and ethical conduct. I also declare that, as required by these rules and conduct, I have fully cited and referenced all material and results that are not original to this work.**

Name Last name : Erdem Mercan

Signature :

# ABSTRACT

## REAL-TIME STABILITY ANALYSIS IN FOOD SYSTEMS WITH MAGNETIC RESONANCE

Mercan, Erdem
Master of Science, Food Engineering
Supervisor: Prof. Dr. Mecit Halil Öztop
Co-Supervisor: Prof. Dr. Rob Morris

August 2024, 97 pages

Food stability has always been the interest of the consumers, food producers and regulatory authorities. It is becoming more significant due to the food safety and food quality issues. In this thesis, the initial part of the study focused on the development and optimization of a portable NMR probe which will be used to analyze food systems. The design process included simulations to optimize the magnetic field homogeneity and strength. Then, this custom-built portable NMR probe was tested through a model food system which consists of sucrose, corn syrup, gelatine and water. Correlations done through a linear regression model show its use to monitor the total soluble solid content (TSS) and correlated it with $T_2^{eff}$ relaxation times. A linear relationship was observed on the plot of data. Regression analysis was performed accordingly. The lack-of-fit test p-value is found to be 0.210 and has a high coefficient of determination ($R^2 = 0.9113$) which shows the model fits well. In the second part, to determine if imaging is necessary to fully understand complex food systems, a benchtop Magnetic Resonance Imaging (MRI) was used to assess the food stability in a model food system which is focusing on pea protein isolate (PPI) mixed with high methoxyl pectin (HMP). Particle size measurements showed that for 2% and 4% PPI containing samples, there is a significant increase ($p<0.05$).

Over the 24-hour observation period, $T_1$ weighted image intensity displayed a statistically significant increasing trend ($p<0.05$). The $T_2$ weighted image intensity shown a significant decrease ($p<0.05$) since the water molecules' mobility is increasingly restricted, due to the tighter network of protein aggregates limiting the free movement of water protons. On the other hand, $T_1$ and $T_2$ Map showed that the locational $T_1$ and $T_2$ relaxations time are decreasing over the duration.

Keywords: Magnetic Resonance, NMR Hardware, Aggregation, Pea Protein Isolates, NMR Relaxometry

# ÖZ

## MANYETİK REZONANS İLE GIDA SİSTEMLERİNDE GERÇEK ZAMANLI STABİLİTE ANALİZİ

Mercan, Erdem
Yüksek Lisans, Gıda Mühendisliği
Tez Yöneticisi: Prof. Dr. Mecit Halil Öztop
Ortak Tez Yöneticisi: Prof. Dr. Rob Morris

Ağustos 2024, 97 sayfa

Gıda stabilitesi her zaman tüketicilerin, gıda üreticilerinin ve düzenleyici makamların ilgi alanı olmuştur. Gıda güvenliği ve gıda kalitesi sorunları nedeniyle daha da önemli hale gelmektedir. Bu tezde, çalışmanın ilk kısmı, gıda sistemlerinin stabilitesini analiz etmek için kullanılacak taşınabilir bir NMR probunun geliştirilmesi ve optimizasyonuna odaklanmıştır. Tasarım süreci, manyetik alan homojenliğini ve gücünü optimize etmek için simülasyonları da içeriyor. Daha sonra, bu özel yapım taşınabilir NMR probu sükroz, mısır şurubu, jelatin ve sudan oluşan bir model gıda sistemi üzerinde test edilmiştir. Doğrusal bir regresyon modeli aracılığıyla yapılan korelasyonlar, toplam çözünür katı içeriğini (TSS) izlemek için kullanıldığını ve $T_2^{eff}$ relaksasyon süreleriyle ilişkilendirildiğini göstermektedir. Verilerin grafiğinde doğrusal bir ilişki gözlemlenmiştir. Regresyon analizi buna göre yapılmıştır. Uyum eksikliği testi p-değeri 0,210 olarak bulunmuştur ve modelin iyi uyum sağladığını gösteren yüksek bir belirleme katsayısına ($R^2$ = 0,9113) sahiptir. İkinci bölümde, karmaşık gıda sistemlerini tam olarak anlamak için görüntülemenin gerekli olup olmadığını belirlemek amacıyla, yüksek metoksil pektin (HMP) ile karıştırılmış bezelye protein izolatına (PPI) odaklanan bir model gıda sisteminde gıda stabilitesini değerlendirmek için bir tezgâh üstü Manyetik Rezonans

Görüntüleme (MRI) kullanılmıştır. Partikül boyutu ölçümleri %2 ve %4 PPI içeren numuneler için anlamlı bir artış olduğunu göstermiştir ($p<0.05$). 24 saatlik gözlem süresi boyunca, $T_1$ ağırlıklı görüntü yoğunluğu istatistiksel olarak anlamlı bir artış eğilimi göstermiştir ($p<0.05$). $T_2$ ağırlıklı görüntü yoğunluğu, su protonlarının serbest hareketini sınırlayan daha sıkı protein agregatları ağı nedeniyle su moleküllerinin hareketliliği giderek kısıtlandığından önemli bir düşüş göstermiştir ($p<0.05$). Öte yandan, $T_1$ ve $T_2$ Haritası, lokal $T_1$ ve $T_2$ relaksasyon sürelerinin süre boyunca azaldığını göstermiştir.

Anahtar Kelimeler: Manyetik Rezonans, NMR Donanımı, Agregasyon, Bezelye Protein İzolatları, NMR Relaksasyonu

To my family and fiancée,

## ACKNOWLEDGMENTS

I owe a huge thanks to my Supervisor, Prof. Dr. Mecit Halil Öztop at METU, for his continuous support, guidance, and expertise. Your mentorship has played a crucial role in my academic and personal development. I am grateful to him for having such a great supervisor. I would like to extend my gratitude to my co-supervisor, Prof. Dr. Rob Morris at Nottingham Trent University. Your insights and approach have been invaluable to my work. Thank you for your patience to my endless questions, for his scientific support and for his friendship.

This thesis could not have been completed without the support of my loved ones. Your support has been my foundation and has helped me reach this milestone. A special thank you to my fiancée, Bensu Melis Çelik. Your patience, love, and constant encouragement have been a source of strength for me. I am incredibly fortunate to have you by my side, and I look forward to all the adventures that lie ahead with you.

I am also thankful to my friends (Özge Güven, Dilara Özcan, Melis Çetin Karasu, Aymelek Uslu, Umur İsmail Tuna and Gözde Özeşme Taylan) who stood by me through the highs and lows, offering their encouragement, motivation, and patience. Your support has meant the world to me. A special thank you to my friend, Melis Çetin Karasu, whose contributions to this thesis were important.

Additionally, I would like to express my gratitude to Dr. Nicasio Geraldi at Nottingham Trent University. Your assistance and support have been incredibly helpful throughout this process.

This project has received funding from the European Union's Horizon 2020 research and innovation programme under grant agreement No 101008228 (project SuChAQuality).

## TABLE OF CONTENTS

## LIST OF TABLES

TABLES

## LIST OF FIGURES

FIGURES

# CHAPTER 1

# INTRODUCTION

## 1.1 Stability in Food Systems

Stability is known as the ability of a food product to preserve its desired composition, sensory attributes, and structural integrity over a period at specific storage environment in food science and engineering. Stability directly affects food products' nutritional value, shelf life, and quality. The formulation, processing, production, packaging and storage conditions of a food product can cause problems by resulting microbiological, physical and chemical changes in the product. Resistance to processes such as phase separation, sedimentation, and molecular interactions can compromise the product's quality and acceptability.

Protein aggregation can compromise the stability of food products and it is commonly seen in high protein containing food products. Additionally, protein aggregation can change the texture of the food product and causes reduction in its overall nutritional value and consumer approval. Additionally, the stability and utilization dimension of food security play an important role in a stable food system and reducing food insecurity (Grote et al., 2021).

### 1.1.1 Phase Separation in Beverages

One issue in maintaining the stability of food in beverages is phase separation. This occurs when different elements within a product like proteins and polysaccharides separate over time. It's not ideal as it shows instability and can affect the texture and appearance of the product which has an impact on how consumers perceive it. For example, soft drinks should ideally stay consistent over months or even years. If phase separation happens quickly, it's a sign of instability that can be managed by

using stabilizing agents and refining formulation and processing methods (Ahern et al., 2023). Proteins in beverages can aggregate due to factors like changes in pH levels, temperature shifts, ionic strength variations or mechanical stresses. These aggregates can interact with components or themselves to form larger particles or networks that can separate from the liquid portion of the product (McClements, 2018).

Plant based beverages, such as those obtained from peas or soy, can exhibit stability problems compared to traditional dairy and meat based alternatives. These beverages can experience a faster rate of phase separation due to the nature of their components and the processes used during processes. Jeske et al., (2017) found that the separation rate in plant based drinks can be up to 14 times faster than in cow's milk and its stability greatly influenced by the plant source, formulation, and presence of stabilizers. Products without additives, favored by some consumers for their clean labels, tend to show poorer stability, highlighting the need for a balance between natural formulations and stabilizers (Asioli et al., 2017). Plant-based beverages are often made by extracting proteins and other components from plants using water and sometimes by enzymes or alkaline treatments. After extraction, the liquid is homogenized and may be fortified with additional ingredients such as vitamins, minerals, and stabilizers. The homogenization and pasteurization processes are critical in producing a stable, homogeneous product. These steps reduce the particle size and help to create stable emulsions, thus preventing separation during storage (Mäkinen et al., 2016).

#### 1.1.1.1 Pea Protein Isolate

Global protein demand is expected to increase significantly in the near future due to the increasing global population (Henchion et al., 2017). High-quality protein is vital for human nutrition, but producing land-based high-quality protein from livestock and poultry poses sustainability challenges. With the global population and per capita meat consumption rapidly increasing, the demand for meat-based protein is

anticipated to rise by approximately 72% between 2013 and 2050 (G. Wu et al., 2014). The growing trend towards plant-based protein sources can be the answer for these questions and concerns. In response to these changes and trends, the food industry is beginning to explore new alternatives to replace animal-based protein. In addition to traditional plant-based proteins like soy, options with functional properties like chickpeas, peas and other pulses are also becoming popular (Ma et al., 2022).

#### 1.1.1.2 Role of Stabilizers in Enhancing Stability

Stabilizers, such as polysaccharides, play an important role in improving the stability of food systems by interacting with proteins and other food components with forming stable complexes. In the study by (Zhang et al., 2023), it was demonstrated that polysaccharides like beta-glucan, low methyl pectin, and chitosan significantly reduced turbidity and centrifugal precipitation in a collagen peptide-fortified cranberry juice under acidic conditions. These interactions help maintain the homogeneity of the beverage and prevent phase separation and extend its shelf life.

Pectin is a natural polysaccharide which is found in the cell walls of plants and it is known for its stabilizing, thickening and gelling properties (Güzel & Akpınar, 2019). It has wide application area in the food industry due to its functional properties as well as potential health benefits. Additionally, pectin is a cost effective and environmentally friendly ingredient as it can be extracted and obtained from various fruit by-products. As shown by Lan and colleagues, the interaction between pectin and proteins, specifically high methoxyl pectin (HMP), can be used to prevent protein aggregation and improve protein functionality (Lan et al., 2018a). It increased the functionality of pea protein by focusing on the biopolymer ratio, the effects of pH, and the concentrations on the formation of soluble complexes between high methoxyl pectin and pea protein.

In a similar way, it’s been studied the stabilization of acidic milk beverages using pectin and have provided insight into the mechanisms by which pectin can prevent protein aggregation in acidic environments (Guo et al., 2021). Learning that pectin can prevent protein aggregation in acidic environments opens new doors to development of stable, protein-rich foods that retain their quality and sensory properties over time.

#### 1.1.1.3 Role of High-Pressure Homogenization (HMP) in Enhancing Stability

Recent advancements in high-pressure homogenization technology, allowing for pressures up to 350–400 MPa, have created new opportunities for improving the stability and sensory characteristics of food products (Patrignani & Lanciotti, 2016)). Studies have also investigated the influence of high-pressure homogenization on particle size and physicochemical properties of whey protein-based emulsions, underscoring the potential of this technique in food product development (Desrumaux & Marcand, 2002). High-pressure homogenization helps produce finer particles, leading to more stable emulsions.

## 1.2 Principles of Magnetic Resonance

The nucleus of an atom consists of protons and neutrons carrying a charge. Certain nuclei, such as hydrogen ($^{1}$H) shows a property known as "spin," and it is determined by the number of protons. Although commonly, refer to this as the nucleus spinning on its axis, it's not a spinning motion. Rather than that, the collective motion of protons and neutrons generates a moment resulting in a local magnetic field, with north and south poles (see Figure 1.1). This magnetic behavior of the nucleus can be used to understand how rotating objects behave. Essentially the nucleus behaves like a bar magnet with its magnetic poles oriented along the theoretical axis it would rotate on if it were spinning physically.

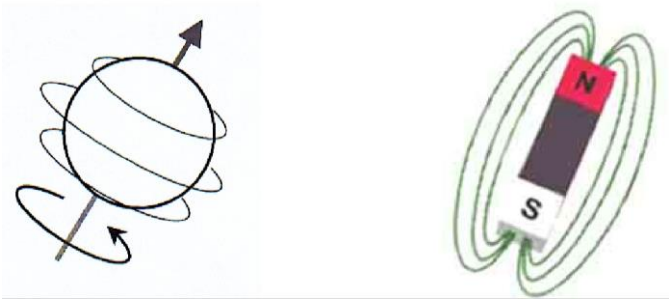


Figure 1.1 Spinning nucleus

When atomic nuclei are exposed to an external magnetic field ($B_0$), the nuclei align either parallel or antiparallel to this field. In a solution containing many nuclear spins affected by the $B_0$ field these spins occupy one of two energy states; a lower energy state which is aligned parallel to the magnetic field, or a higher energy state which is aligned antiparallel to it. For NMR to be possible more spins must in the higher energy state (see Figure 1.2). This quantum description of NMR is useful but can be challenging to understand from the point of view of most NMR experiments. Instead, we think only about the spins which are aligned antiparallel and consider their angle to the $B_0$ field.

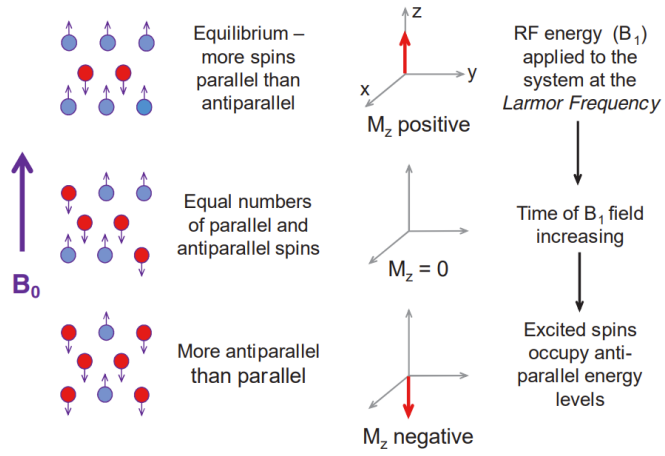


Figure 1.2 Nuclear spin alignment in external magnetic field

Due to its angular momentum, the nucleus exhibits rotational movement known as precession around the $B_0$ axis (Figure 1.3). Even when aligned, this precession is similar to the wobbling motion of a gyroscope influenced by Earth's gravity. The speed at which the nucleus rotates around the magnetic field direction is termed as the Larmor frequency. This frequency is directly correlated with the intensity of the applied magnetic field and is represented by the Larmor equation.

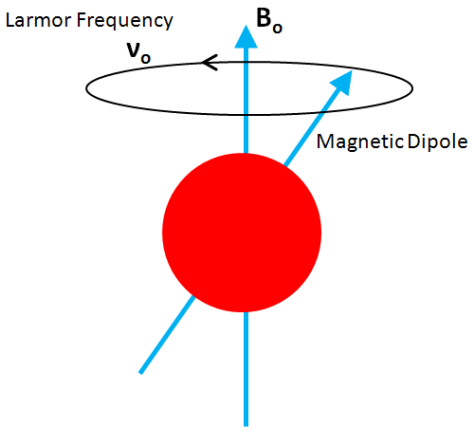


Figure 1.3 Precession of a nucleus

We collect the signal from an NMR experiment from spins which are precessing. When the longitudinal magnetization is disrupted by a radio frequency (RF) pulse of the identical frequency, the system reaches a state of resonance, and the magnetization is reversed to the x-y plane. It disrupts the equilibrium alignment with the external magnetic field $B_0$. Then, nuclei start to precess around $B_0$ at their characteristic Larmor frequency and creates an oscillating magnetic field. This oscillation generates a detectable signal known as Free Induction Decay (FID). The FID signal starts strong but rapidly diminishes due to spin-spin relaxation ($T_2$*) and dephasing which is caused by local magnetic field variations (Ridgway, 2015).

To refocus the dephasing spins and recover the signal, a spin echo sequence is employed. This sequence, which is known as the Hahn echo sequence, was

developed by Erwin Hahn. It starts with applying a 90-degree RF pulse to tip the spins into the transverse plane. Then, another 90-degree RF pulse at a specific time interval ($\tau$) is applied. The second 90-degree pulse flips the spins and cause the spins to refocus and produce an echo signal at time $2\tau$. This spin echo technique compensates for inhomogeneities in the magnetic field and allows for the measurement of $T_2$ relaxation times more accurately. Further improvements to the sequence are discussed in the section 1.4.

## 1.3 NMR Hardware

Some of the important components of NMR hardware such as magnet of the probe, RF coils and its design, tuning and matching circuit, and the spectrometer unit are discussed in the following section.

### 1.3.1 Magnets

A neodymium magnet, also called NdFeB, NIB or Neo magnet is a type of rare earth magnet. These magnets are metallic in nature. Typically has a silver color similar to other metals. The grading of neodymium magnets is based on their energy level, which determines the magnetic flux output per unit volume. Stronger magnets are indicated by values ranging from N35 to N52.

The design of permanent magnets for NMR sensors has a balance between generating a strong magnetic field and providing high field homogeneity within a volume. When using permanent magnets, Halbach arrays are often used in portable low-field NMR devices because of their favorable properties including lack of stray field and compatible field direction with solenoid coil which is perpendicular to each other. This design can achieve high field strength in a small and cheap way (Soltner & Blümler, 2010). Additionally, there are simpler forms of permanent arrays, such as the NMR-MOUSE (Mobile Universal Surface Explore) (Blümich, 2019). The configuration of NMR-MOUSE is usually a bar magnet or u-shaped. The design has

such a shape due to achieve a small, localized homogeneous area which is on the surface or near surface region.

Another type of magnet is superconducting magnet. These magnets have zero electrical resistance and provide expulsion of magnetic field when cooled below critical temperature. That is why superconducting magnets can carry large amounts of electric currents without losing energy and create strong magnetic fields. Common material used in superconducting magnets are niobium-titanium (NbTi) and niobium-tin (Nb3Sn) and magnet system usually has a liquid helium cooling system. (Laukien & Tschopp, 1993).

### 1.3.2 Coils and Tuning Matching Circuits

In NMR spectrometers RF coils have two roles; sending RF pulses to excite the nuclear spins in the sample and picking up the signals released as these spins return to their normal state. When transmitting, the RF coil creates a field perpendicular to the NMR magnet's primary static magnetic field. This field causes the nuclei to resonate at a frequency based on the strength of the static field. The effectiveness of delivering RF energy to the sample is directly impacted by how designed and high quality the RF coil is. Coils are usually tailored for frequencies and adjusted to optimize the transfer of RF power, to the sample.

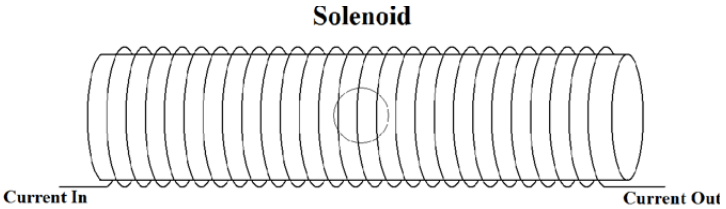


$$v = \frac{1}{2\pi\sqrt{LC}}$$

Figure 1.4 Solenoid type RF coil and design equation

The resonant frequency ($\boldsymbol{\nu}$) of an RF coil is primarily determined by its inductance (L) and capacitance (C) which represent its combined reactance characteristics (Figure 1.4). This resonance is important to provide accurate and effective magnetic resonance applications.

### 1.3.3 Spectrometers

The spectrometers generate RF pulses which are transmitted into the sample through the NMR probe which has the magnetic field. These pulses disturb the orientation of the nuclei and start the NMR signal generation process (Blümich et al., 2002). After the excitation, the spectrometer switches to signal reception mode. It collects the NMR signals emitted by the nuclei while nuclei return to their equilibrium state. These signals are amplified, digitized, and processed to create the NMR spectra. Then, signal can be analyzed for detailed molecular information (Gan et al., 2008).

## 1.4 Carr-Purcell-Meiboom-Gill (CPMG) pulse sequence

Hahn also noticed that in an inhomogeneous field, the effects of random translational diffusion during $\tau$ was not corrected by the second pulse and contributed to the decay of the spin echo. In response, Carr and Purcell in 1954 showed that a 90° pulse followed by a ($\tau$−180°−$\tau$) in pulse train will restrain the effect of diffusion if the $\tau$ delay is adequately short. Moreover, they realized that by measuring each resulting echo that occurring between successive 180° pulses, a complete $T_2$ relaxation data set can be attained in a single experiment. In 1958, Meiboom and Gill improved this technique by utilizing better electronics to generate coherent pulses with the initial 90° pulse shifted in phase by 90° relative to the subsequent 180° pulses. This modification effectively counteracted the cumulative imperfections of the 180° pulses throughout the pulse train.

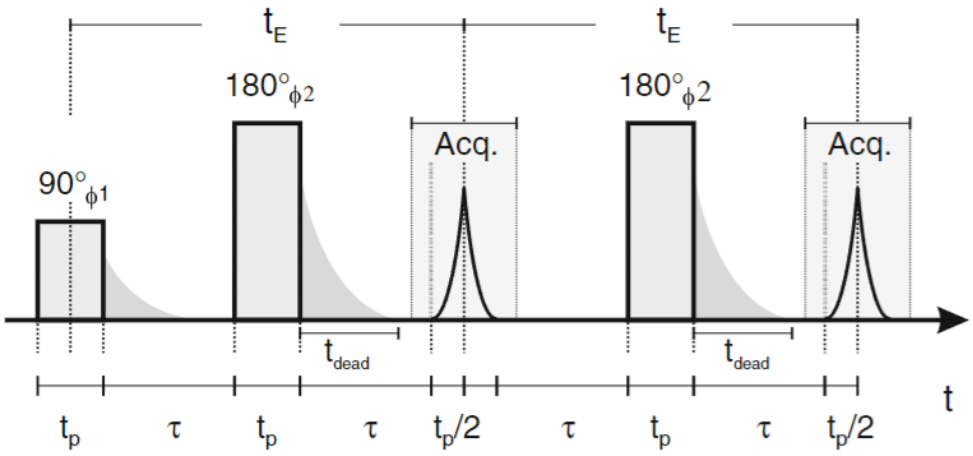


Figure 1.5 Carr-Purcell-Meiboom-Gill (CPMG) pulse sequence

$T_2$ relaxation refers to the decay or dephasing of the transverse components of magnetization ($M_{xy}$) and $T_2$ time represents the duration it takes for the transverse magnetization to decrease to about 37% (1/e) of its original magnitude (Chavhan et al., 2009). For inhomogeneous fields, many factors including diffusion and residual gradients also impact this dephasing and thus the expected refocusing of the echoes is not perfect and they will decay more rapidly. We therefore call the envelope over the peaks of the train of echoes as the effective $T_2$ ($T_2^{eff}$) where the decay is given by:

$$S(t_E) = S_0 \exp\left(-\frac{t_E}{T_2} - \frac{1}{12}\gamma^2 G_0^2 D (t_E)^3\right).$$

Figure 1.6 The decay of $T_2^{eff}$ (Casanova et al., 2011).

## 1.5 Image Acquisition

Magnetic Resonance Imaging (MRI) is an emerging non-destructive examination method that used to study the properties of foods without any harmful interference

with the components of biological matter and quality (Aboonajmi & Faridi, 2016). MRI plays an important role in quality control and verification of food authenticity for the food industry (Kirtil & Oztop, 2016). MRI creates 2D or 3D visual representations by using magnetic gradient coils and collecting spatial information. The spatial details acquired from the signal exhibit changing contrasts, allowing us to obtain significant information about the interactions of food samples and internal structure (Ozel & Oztop, 2021). It allows a variety of measurements that contribute to the understanding of quality parameters, maturity, and the physiological processes underlying these factors. MRI's ability to encode molecular dynamics through different contrast mechanisms and work non-destructively has enabled its widespread application in assessment of food quality and post-harvest processing (Patel et al., 2015).

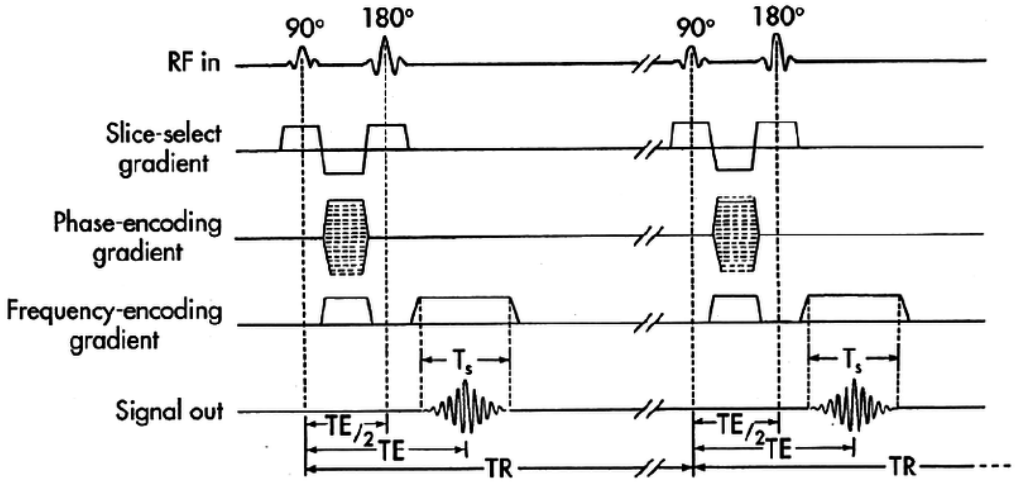


Figure 1.7 2D Spin Echo Pulse Sequence.

Figure 1.7 demonstrates the 2D spin echo sequence for generating two-dimensional images. The sequence involves important components: radiofrequency (RF) pulses, slice-select gradient, phase-encoding gradient, and frequency-encoding gradient.

The sequence begins with a 90° RF pulse, which tips the magnetization into the transverse plane. This is followed by a 180° RF pulse applied after a time interval TE/2, which refocuses the spins and creates an echo at time TE (echo time)(Jung & Weigel, 2013). The phase-encoding gradient (PEG) is applied after the slice-select gradient and before the signal readout. This gradient is varied incrementally with each repetition time (TR) to encode spatial information in the second dimension. The application of different gradient strengths causes a phase shift in the spins, which is dependent on their position along the phase-encoding direction. This phase shift allows for the spatial localization of the signal in the second dimension.

The Spin echo sequence needs to be repeated to acquire the chosen matrix size $N_P$ in the phase-encoding direction since only one phase encoding gradient can be applied per TR.

### 1.5.1 Repetition Time (TR) and Echo Time (TE)

TR (repetition time) is an important parameter in magnetic resonance imaging (MRI) that significantly influences the quality and characteristics of the images produced (Seeger, 1989). It is a fundamental MRI parameter that must be set appropriately so that the time it takes for the protons to return to their equilibrium state following a radiofrequency excitation pulse. Short TR values result in faster image acquisition but may lead to reduced signal, while longer TR values allow for better signal but increase the overall scan time (Wilkinson-Smith et al., 2018).

TE represents the time interval between the application of the radiofrequency pulse and the peak of the echo signal received from the tissue being imaged. It is a crucial parameter that influences the contrast and characteristics of the images produced (Plewes, 1994). Adjusting TE (echo time) and TR (repetition time) provide significant adjustments on images. The impact of TE and TR extends to various MRI sequences and applications, including $T_1$ weighted, $T_2$ weighted, and diffusion-

weighted imaging, where the manipulation of these parameters influences image contrast.

Table 1.1 MRI Parameters: TR and TE in Different Weighting Techniques

| **Weighting** | **Repetition Time (TR)** | **Echo Time (TE)** | **Contrast Characteristics** |
|---|---|---|---|
| **$T_1$-weighted** | Short | Short | High $T_1$ contrast: Tissues with different $T_1$ relaxation times are distinguishable. |
| **$T_2$-weighted** | Long | Long | High $T_2$ contrast: Tissues with different $T_2$ relaxation times are distinguishable. |
| **PD-weighted** | Long | Short | Low $T_1$ and $T_2$ contrast: Emphasizes proton density, providing uniformity |

### 1.5.2 Contrast Agent used in MRI Field

Contrast agents are popular in Magnetic Resonance Imaging due to its use to improve contrast difference between different regions (Yan et al., 2007). Most common contrast agents that are available in the industry are dysprosium ($Dy^{3+}$), gadolinium ($Gd^{3+}$), or manganese ($Mn^{2+}$) (Xiao et al., 2016).

In biological environments, the mediums which consist of protein, water, and other components lead to a wide range of relaxation times, which are quite important for

generating contrast. Paramagnetic ions ($Gd^{3+}$, $Fe^{2+}/Fe^{3+}$, $Mn^{2+}$) dissolved in these aqueous environments and act as strong microscopic magnets. As water protons come close to these ions, typically within 0.1 to 1 nanometer, they experience intense magnetic interactions that cause them to relax almost instantly. These protons are then quickly replaced by unrelaxed water molecules, thereby influencing the overall average relaxation times within the voxel (Hao et al., 2012). In this way, those agents help to achieve desired contrast within the image.

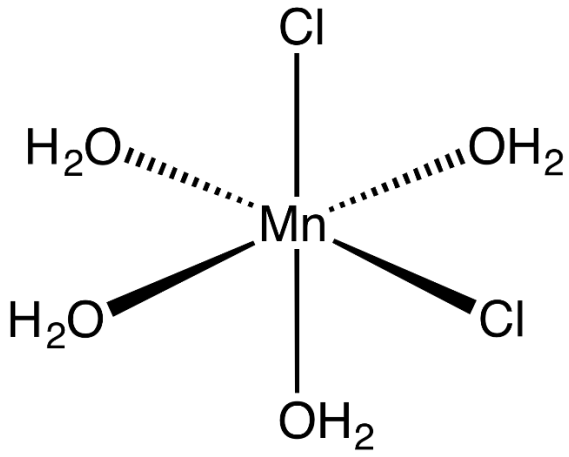


Figure 1.8. Molecular structure of $Mn_2Cl$

## 1.6 Objective of this study

This thesis consists of two parts. The primary aim of the first part is to build a portable NMR probe and to test its use for complex food sample analysis through a model food system. The second part, on the other hand, aims to investigate if imaging is necessary to fully understand complex food systems through using a benchtop Magnetic Resonance Imaging (MRI) to assess the food stability in a model food system which is focusing on pea protein isolate (PPI) mixed with high methoxyl pectin (HMP).

- To design and construct a portable NMR probe for benchtop and in-line applications for analyzing food systems to collect accurate structural information of food samples.
- To do an optimization and set necessary parameters of the portable NMR.
- To observe the time-dependent aggregation behavior of PPI in a model food system.
- To assess the impact of aggregation on the structural changes and stability of the food matrix over using imaging techniques such as $T_1$ and $T_2$ weighted spin echo imaging, $T_1$ mapping, and $T_2$ mapping using benchtop MRI.
- To quantitatively analyze changes in signal intensities and relaxation times as indicators changes within the food matrix which includes water mobility and protein network formation.

# CHAPTER 2

# MATERIALS & METHODS

The initial part of the study focused on the development and optimization of a portable NMR probe which will be used to analyze food systems. Then, this custom-built portable NMR probe is tested through a model food system which consists of sucrose, corn syrup, gelatine and water. In the second part of the study, Magnetic Resonance Imaging (MRI) techniques were used to assess food stability through a model food system.

## 2.1 Design of Portable NMR device and its testing

The steps to design the NMR probe are discussed in the following sections.

### 2.1.1 Portable NMR device design and Optimization

The design and optimization process must be completed for the magnet arrangement, RF coil and tuning, spectrometer and shielding which are discussed in the following sections.

#### 2.1.1.1 Magnet Design and Optimization

The first thing completed for the NMR probe is the magnet part. The selected design for the NMR probe's magnet part is based on a Halbach array configuration, which is widely recognized for its ability to generate a highly uniform magnetic field. This uniformity is crucial for obtaining precise and reliable nuclear magnetic resonance (NMR) readings, particularly when assessing the properties of food samples. The development process of this NMR probe involved meticulous planning and

simulations using finite-element method (FEM)-based software, which allowed for the optimization of the magnetic field homogeneity and the overall performance of the device. The type of magnet used here is N42 NdFeB magnets and its dimensions are 5mmx8mmx130mm.

**Simulation of Halbach Array Designs:**

Table 2.1 Radius of Simulated Halbach Array Designs

| Design Number | Radius (mm) |
|---|---|
| **1** | 22 |
| **2** | 24 |
| **3** | 26 |
| **4** | 28 |

To optimize the NMR probe design, four different Halbach array configurations were simulated. Each configuration varied by the radius of the Halbach array from the center of the array. The radius used for these simulations were 22 mm, 24 mm, 26 mm, and 28 mm. This range was selected to explore the effects of different spatial distributions of the magnetic field on the performance of the probe.

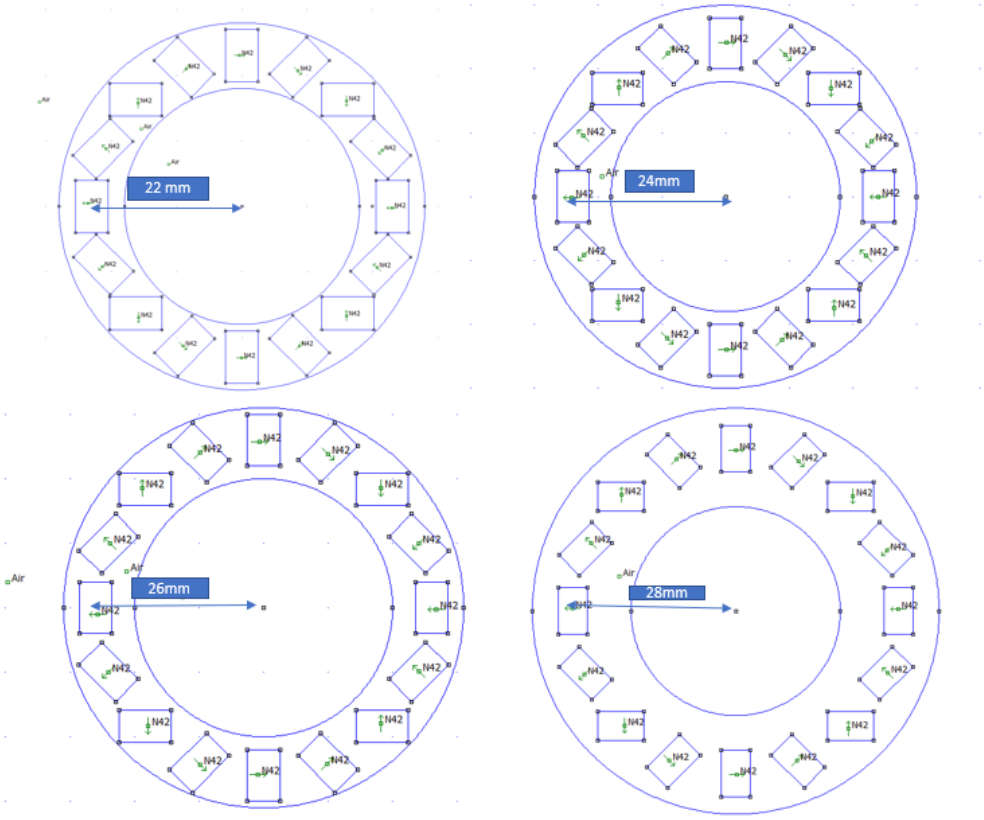


Figure 2.1 Halbach Array Configurations for Portable NMR Device: (a) 22mm radius, (b) 24 mm radius, (c) 26 mm radius, (d) 28 mm radius.

The goal of these simulations was to assess the homogeneity and strength of the magnetic field generated by each configuration. By analyzing these variables, the design could be optimized to ensure that the field is both sufficiently strong and uniform across the sample area. This is particularly important in NMR applications where variations in the magnetic field can lead to inaccuracies in the measurement of relaxation times ($T_1$ and $T_2^{eff}$) and other critical parameters.

**Field Analysis:**

The fields generated by these designs were analyzed using the FEM-based software, with a particular focus on achieving the most homogeneous field possible. The magnetic field ($B_0$) and magnetization change were the primary points of focus during this analysis.

A)

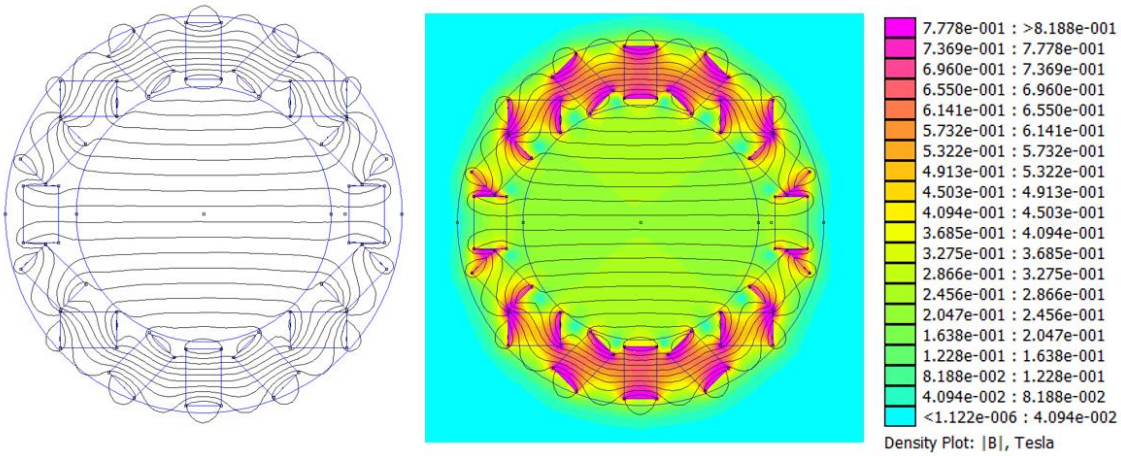
7.778e-001 : >8.188e-001
7.369e-001 : 7.778e-001
6.960e-001 : 7.369e-001
6.550e-001 : 6.960e-001
6.141e-001 : 6.550e-001
5.732e-001 : 6.141e-001
5.322e-001 : 5.732e-001
4.913e-001 : 5.322e-001
4.503e-001 : 4.913e-001
4.094e-001 : 4.503e-001
3.685e-001 : 4.094e-001
3.275e-001 : 3.685e-001
2.866e-001 : 3.275e-001
2.456e-001 : 2.866e-001
2.047e-001 : 2.456e-001
1.638e-001 : 2.047e-001
1.228e-001 : 1.638e-001
8.188e-002 : 1.228e-001
4.094e-002 : 8.188e-002
<1.122e-006 : 4.094e-002
Density Plot: |B|, Tesla

B)

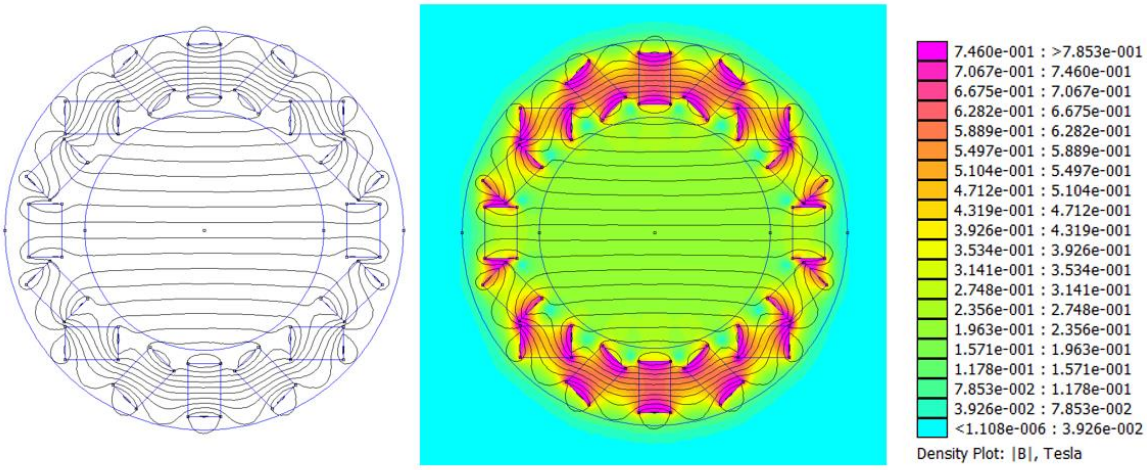
7.460e-001 : >7.853e-001
7.067e-001 : 7.460e-001
6.675e-001 : 7.067e-001
6.282e-001 : 6.675e-001
5.889e-001 : 6.282e-001
5.497e-001 : 5.889e-001
5.104e-001 : 5.497e-001
4.712e-001 : 5.104e-001
4.319e-001 : 4.712e-001
3.926e-001 : 4.319e-001
3.534e-001 : 3.926e-001
3.141e-001 : 3.534e-001
2.748e-001 : 3.141e-001
2.356e-001 : 2.748e-001
1.963e-001 : 2.356e-001
1.571e-001 : 1.963e-001
1.178e-001 : 1.571e-001
7.853e-002 : 1.178e-001
3.926e-002 : 7.853e-002
<1.108e-006 : 3.926e-002
Density Plot: |B|, Tesla

C)

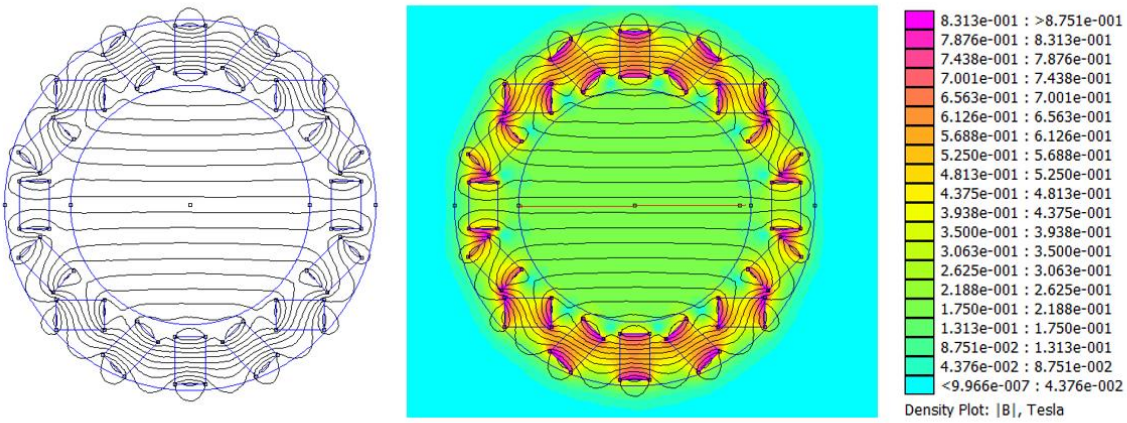


D)

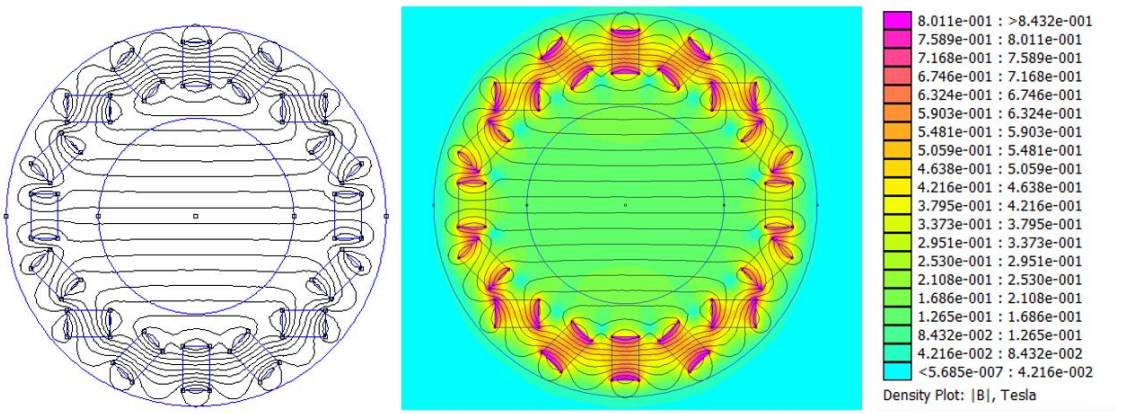


Figure 2.2 Magnetic Field Simulation in a Halbach Array for Portable NMR Device (A) 22 mm radius, (B) 24 mm radius, (C) 26 mm radius, (D) 28 mm radius.

To analyze the magnetic field distribution, a line was drawn through the center of Halbach array configuration. After that, the field strength (in Tesla) was plotted against the length inside the probe. This analysis helps in understanding how the

magnetic field varies across the space between the magnet's arrays. Based on the analysis of magnetic field homogeneity in various Halbach array configurations, it was determined that the design with a 26 mm radius using 16 magnets provided the most uniform magnetic field (Figure 2.3). Because of this optimal performance, the 26 mm radius Halbach array was selected as the standard to build the magnet.

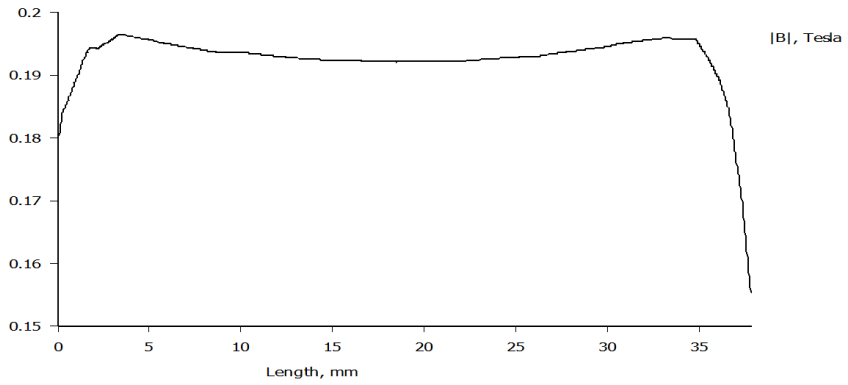


Figure 2.3 Field (Tesla) vs. Length Inside the Halbach Array

The design and optimization of the NMR probe using a Halbach array with a 26 mm radius configuration have been shown to provide a uniform magnetic field which are the constructed using laser cut acrylic sheets to the dimensions shown in Appendix A, bonded with one-part acrylic bonder, and magnets inserted one at a time.

Figure 2.4 Cropped Photograph of Crafted NMR Probe with covered with copper foil

Figure 2.4 shows the actual Halbach array magnet crafted according to the design specifications (a comprehensive dimensional schematic can be found in Appendix A). The array is wrapped in copper foil to reduce noise which is discussed further in Section 2.1.1.4.

#### 2.1.1.2 Radiofrequency (RF) Coil Design and Tuning and Matching Circuit

RF coils have an important role in magnetic resonance imaging (MRI) procedures. They have the task of creating RF fields to stimulate the nuclei in the sample and capturing the RF signals emitted by these nuclei (Giovannetti et al., 2024). It is important when designing RF coils for MRI to be sure that the coil is precisely calibrated to resonate at the Larmor frequency of the nucleus being studied (Gruber et al., 2018). Solenoid type coils, commonly utilized in RF coil design are designed to generate the $B_1$ field for a pulse sequence and detect precession in the x-y plane (Sun et al., 2020). Solenoid coils which are illustrated on Figure 1.4 are favored for their ability to offer localized transmit/ functions, like $B_1$ homogeneity.

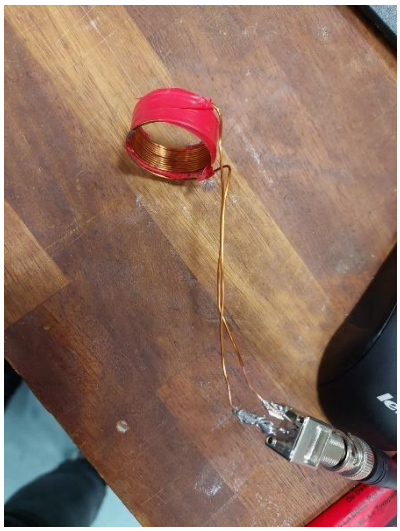

Figure 2.5 The solenoid coil build for the system

Figure 2.5 shows a solenoid RF coil which is built for the portable NMR system. This coil is 26 mm diameter and 15 turns. The variable capacitor on the circuit (Figure 2.6) provides to do some adjustment to $B_1$ field which is generated by the solenoid design. It is quite important for the accurate signal from NMR data since it is gives a prior calibration and improvement to $B_1$ field to the system.

Figure 2.6 A photograph of the circuit used in this system

### 2.1.1.3 Spectrometer

After assembly, the sensor and tuning circuit were integrated with a KEA$^2$ Spectrometer from Magritek, New Zealand. This spectrometer was operated using the Prospa software, also developed by Magritek, ensuring control and functionality.


Figure 2.7 KEA$^2$ spectrometer that is used in the NMR probe system

### 2.1.1.4 RF Shielding

In the system a radiofrequency shield was also introduced to the system to improve Signal to noise ratio. It helps to neglect the noise which existed in the environment due to signals of the different kinds of electronics. An enclosure made using copper plated board formed an RF Shield in this NMR probe system.

The effectiveness of the RF shield is texted with glycerol. CPMG pulse sequence was run with RF shield, and it also run without it. The results of this experiment shown in Figure 2.8. The left graph shows the results without RF shielding, while the right graph shows the results with RF shielding. It is clear that RF shield is effective for improving measurement accuracy through increasing Signal-to-Noise.

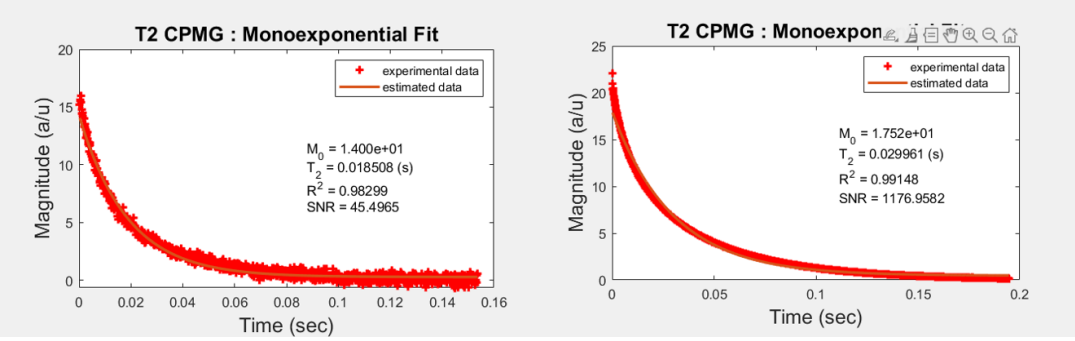


Figure 2.8 Comparison of CPMG Pulse Sequence with and without RF Shielding.

#### 2.1.1.5 Tuning of Portable NMR Device

Proper tuning of the RF coil aligns the probe circuitry to the desired transmit frequency, while matching ensures that maximum power is transmitted to the coil with reflections. This calibration process usually involves the use of a network analyzer to generate a 'curve'. A network analyzer measures network characteristics such as dispersion parameters including reflection and transmission.

When you connect a network analyzer, the wobble curve shows the strength of the signal bouncing back at different RF frequencies. You adjust the tuning and matching parts by looking at this curve, aiming to align the point on the curve exactly with the resonance frequency of your sample when it is in the $B_0$ magnetic field. You also want the dip to be longer to show that there's hardly any reflection and to make sure that the power goes smoothly to the coil.

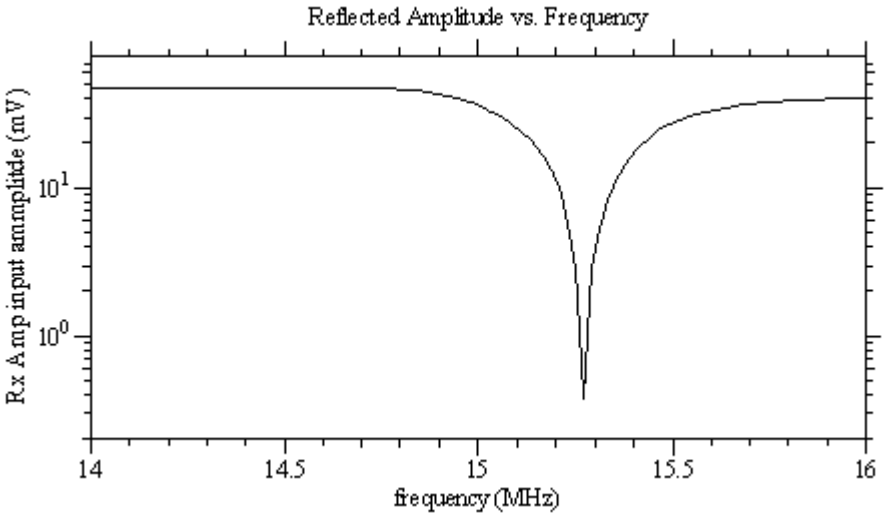


Figure 2.9 Example of wobble

After portable NMR device parts were completed and compiled together, it needs some adjustments. $B_1$ field, which is the field generated by the RF coil is observed by network analyzer Figure 2.9 and matching of the frequency was done through the readjustment of the variable capacitor on the circuit which shown in Figure 2.6.

### 2.1.2 Calibration Protocol Before Experiments

After the hardware of the NMR probe is completed, the next step is calibration of the parameters for experimental procedures to get optimal results.

#### 2.1.2.1 CPMG Duration Sweep

The goal is to find the pulse lengths for NMR by adjusting the RF pulse duration. The pulse sequence “CPMG Duration Sweep” was used in a way that a CPMG sequence is performed at different pulse durations. Once all echoes are gathered a Fourier transformation is applied and then, the peak integral of the transformed data is graphed and recorded.

Optimal pulse durations are crucial for NMR calibration. Determination of 90 degree and 180-degree pulse durations are quite important to achieving a good performance by maximizing signal strength and clarity. This calibration improves SNR as well.

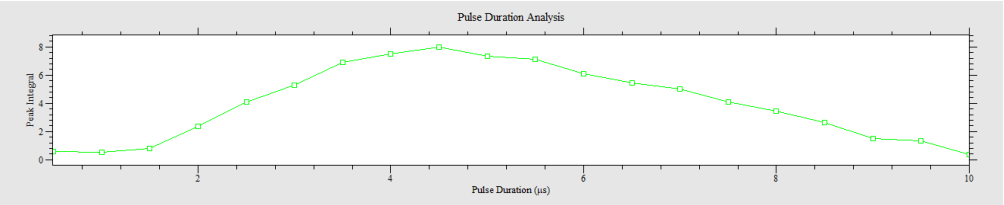


Figure 2.10 CPMG Pulse Duration Sweep for Magnet Calibration

Figure 2.10 displays the Pulse Duration in microseconds (µs) on the x axis and the Peak Integral of the NMR signal on the y axis. As the pulse duration goes up from 0 to 10 µs, there is an increase in the peak integral which means that the RF pulses are getting better at exciting the nuclear spins. The first noticeable point on the graph is a peak around 4.8 µs, which corresponds to the duration for a 90-degree pulse. At this point the RF pulse effectively flips the magnetization vector into the plane leading to a strong NMR signal.

After this peak there is a decline towards a minimum at 10 µs. This minimum marks the duration for a 180-degree pulse that flips the magnetization vector by 180 degrees to realign spins and create a spin echo. Beyond this point as pulse duration increases further there is a decrease in peak integral indicating that longer pulses might be less efficient or could exceed optimal conditions, for flipping by 180 degrees.

#### 2.1.2.2 CPMG Frequency Sweep Pulse Sequence

In the CPMG Frequency Sweep experiment, the $B_1$ frequency is changed in the sequence to find the optimal NMR resonant frequency as the example can be seen in Figure 2.11. This method includes CPMG co-adding of echoes to enhance the SNR. The summed echoes undergo Fourier transformation, and the resulting peak integral

is plotted. The first maximum in the curve indicates the 90-degree pulse duration, while the first minimum identifies the 180-degree pulse duration.

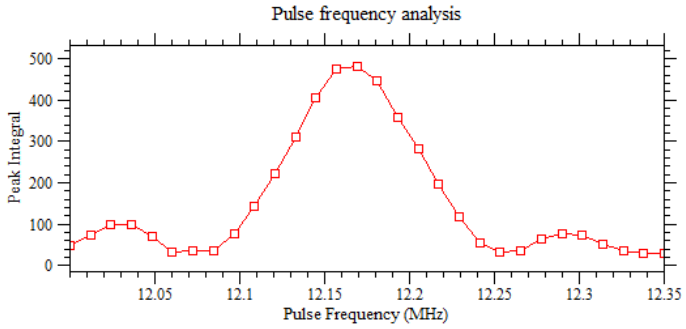


Figure 2.11 Example Pulse Frequency Analysis

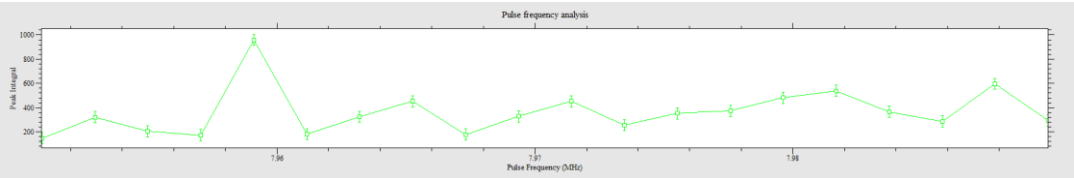


Figure 2.12 Pulse Frequency Analysis of portable NMR system which is built

The final $B_1$ field frequency is decided here as close to 9.957 MHz. There is a slight deviation from the simulation results because of environmental factors and the simulation tool incapabilities.

### 2.1.3 Testing of the custom-built portable NMR system

#### 2.1.3.1 Sample Preparation

A gelatin solution is prepared with 8g powdered gelatin mixed in 16g of hot water at 90 °C and let cool to room temperature. Gelatin is cut into smaller pieces after

cooling. Then, 20g corn syrup and 40g of sucrose were heated in 20ml water until the temperature reached 100°C at 300 rpm and 200°C on a hot plate. Next, gelatin added on sugar mixture and mixed for 15 minutes to dissolve it at 300 rpm and 200°C. Then, after that every 2 minutes a sample is molded and kept at room temperature.

#### 2.1.3.2 Total Soluble Solid (TSS) Content Measurement

TSS is an important parameter in production, as it impacts the texture, flavor, and shelf-life of the product. The model food system which is trying to simulate a heating process on a model food system. The aim of TSS measurement is to quantify TTS values at different intervals of heating process. Samples are taken away every 2.5 minutes. TSS measurements are taken before it is cooled. In this way, concentration of soluble solids change can be observed over time.

The TSS values of samples were determined using a benchtop digital refractometer (Hanna Instruments, Rhode Islands, USA), which is a standard tool for measuring the TSS in food products. A small amount of each sample was placed on the surface of the refractometer. Three replicates are used for each sample.

#### 2.1.3.3 The CPMG (Carr-Purcell-Meiboom-Gill) $T_2^{eff}$ Experiment

The Custom-built Halbach array magnet is used with the Magritek KEA$^2$ spectrometer as previously described. The spacing was optimized using finite element simulations (FEMM, femm.info) and comprises 16 NdFeB magnets. The magnetic field in the homogeneous region is 0.192T. Samples are measured with Carr-Purcell-Meiboom-Gill (CPMG) to improve signal to noise ratio.

To test the Halbach array magnet, the following parameters set to be input into the software for the CPMG (Carr-Purcell-Meiboom-Gill) $T_2^{eff}$ experiment to perform the experiments on the model food system.

Table 2.2 Parameters for the CPMG (Carr-Purcell-Meiboom-Gill) $T_2^{eff}$

| **Parameter** | **Value** |
|---|---|
| Repetition Time | 500 ms |
| Echo time | 95 μs |
| Number of Echoes | 2048 |
| Number of averages | 64 |
| $B_1$ Frequency | 9.957 MHz |

## 2.2 Uses of a Benchtop MRI system to investigate food stability through a model food system

The steps needed to investigate food stability are described in this section including sample preparation, appropriate hardware and experimental details.

### 2.2.1 Sample Preparation

Samples were first prepared by high pressure homogenizing a mixture consisting of high methoxyl pectin, pea protein isolate, and water under high pressure which is at 500MPa. While the concentration of high methoxyl pectin was kept constant at 0.5%, three different groups were formed with concentrations of pea protein isolate at 4%, 2%, and control group. After the homogenization step, $MnCl_2$ was added to each sample at a concentration of 0.1 mM. It is used as a contrast agent, promoting the visualization of protein aggregates during Magnetic Resonance Imaging (MRI). Including $MnCl_2$ as a contrast agent is an important contribution to the experiment, allowing for a better understanding of the spatial distribution and behavior of protein aggregates when visualized with benchtop MRI techniques. After adding $MnCl_2$, the samples, categorized into three groups with pea protein isolate concentrations of 4%,

2%, and a control group (no protein), were tested at time points of 1 hour, 3 hours, 7 hours, and 24 hours to observe stability dynamic over time which is affected by protein aggregation and sedimentation.

### 2.2.2 2D Magnetic Resonance Imaging Experiments

A benchtop MRI system from Pure Devices GmbH (Germany) is used for imaging experiments. The probe of benchtop MRI system is operating at a proton resonance frequency of 24.15 MHz. The equipment has a gradient amplifier capable of delivering maximum gradient strengths of 1.229 T/m in the x-axis, 1.230 T/m in the y-axis, and 1.515 T/m in the z-axis, and includes a 10 mm RF coil. For 2D imaging acquisition procedure, the software interface, developed in MATLAB PD_Imaging_GUI_V_Alpha by McCarthy Engineering (Davis, U.S.A.) was used.

#### 2.2.2.1 2D Spin Echo Imaging

During image acquisition, a gradient echo sequence was used with specific repetition time (TR), echo time (TE), number of scans (n) values which are adjusted according to the sample type and imaging requirements. These values were chosen according to the $T_1$ (ms) and $T_2$ (ms) relaxation values of the samples. The number of scans value was determined as 1 to shorten the experiment time because the samples had long $T_1$ relaxation times and a very dynamic structure and sufficient signal is acquired without averaging.

The following parameters are required to be input into the software for the imaging process:

Table 2.3. MRI Parameters for 2D Spin Echo sequence

| | $T_1$ weighted Spin Echo Images | $T_2$ weighted Spin Echo Images |
|---|---|---|
| Number of averages | 1 | 1 |
| TE (ms) | 5 | 60 |
| TR (ms) | 300 | 2500-3000 |
| Slice thickness | 5 | 5 |
| FOV(mm) | 12,8 | 12,8 |

#### 2.2.2.2 $T_1$ Mapping

At the start, a 90° pulse RF pulse that rotates the magnetization into the transverse plane. Following this excitation, a recovery time $T_{sat}$ is set during which the magnetization recovers along the z-axis toward its equilibrium state. A standard spin echo sequence is then performed. To determine $T_1$, $T_{sat}$ is varied across different repetitions. By using a range of $T_{sat}$ values, the sequence obtains signals at which the magnetization is at different stages of recovery. This creates a dataset similar to the $T_1$ relaxation behavior. To generate a $T_1$ map images are taken at intervals of $T_{sat}$. These images are then analyzed to fit the recovery curves of each voxel with a $T_1$ relaxation model. This process creates a spatial map showing $T_1$ relaxation times throughout the sample.

The following parameters are required to be input into the software for the imaging process:

Table 2.4 Parameter of $T_1$ Mapping Pulse Sequence

| | Parameter | Value | Description |
|---|---|---|---|
| | $T_1$ estimated | 300-600ms | Estimated $T_1$ of the sample. |
| | Sequence type | Saturation | Type of recovery pulse ('Saturation' or 'Inversion'). |
| | Number of loops | 7 | Number of loops. |
| | Echo time | 4 ms | Echo time in seconds. |
| | Image size | 0.0096 m | Image size in the read direction. |
| | Slice thickness | 5 mm | Slice thickness (also third dimension which is averaged). |

#### 2.2.2.3 $T_2$ Mapping

A Spin Echo (SE) pulse sequence designed for Magnetic Resonance Imaging (MRI) optimized for mapping $T_2$ relaxation times used for $T_2$ mapping. The fundamental principle of this sequence involves using a series of radio frequency (RF) pulses along with adjustments to realign magnetic spins and generate echoes. It begins with a 90° RF pulse that shifts the net magnetization vector to the plane followed by a sequence of 180 degree refocusing pulses. The Echo Time (TE) which represents the time between the 90° pulse application and the peak of the echo plays a role in determining the $T_2$ relaxation times in the resulting image. This procedure uses an array of echoes produced by 180° pulses at varying intervals to create a $T_2$ weighted image as an imaging equivalent of the CPMG sequence described in section 1.4. The

length of the echo train and the Repetition Time (TR) are adjusted based on the estimated $T_2$ value of the sample.

The following parameters are required to be input into the software for the imaging process:

Table 2.5 Parameter of $T_2$ Mapping Pulse Sequence

| Parameter | Value | Description |
|---|---|---|
| $T_2$ Estimated | 100-200 ms | Estimated $T_2$ value of the sample. (changed it according to treatment to the mixtures) |
| Number of Loops | 1 | Number of loop averages. |
| Echo Time | 2.5 ms | Echo time in seconds. |
| Size | 10 mm | Image size in on both plane. |
| Thickness | 3 mm | Slice thickness (also third dimension which is averaged). |

### 2.2.3 Analysis of Magnetic Resonance Images

The software used for imaging applications is MATLAB based software. When an image is acquired through spin echo pulse sequence. Resolution of the image can be changed according to achieve a good SNR (signal to noise). 32x32, 64x64, and 128x128 resolution MATLAB images can be obtained. An example of the image given in Figure 2.13.

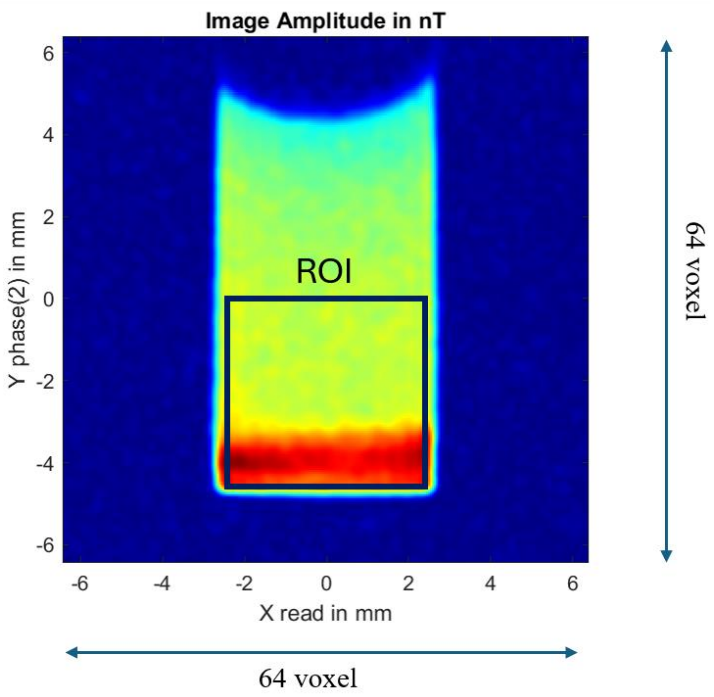


Figure 2.13 Example image of $T_1$-weighted spin echo image(64x64)

The MATLAB-based software is used to do the analysis of MRI data. It starts by defining the position and size of the ROI. The ROI is a selected area within the image. In the code, the ROI is specified using coordinates and dimensions that define a rectangular region within the image.

The next step involves extracting a sub-region from the image based on the defined ROI which is seen in the given figure. This sub-region is then analyzed to calculate various metrics (mean, std) that describe the pixel intensities within the ROI. The average intensity value of all pixels within the ROI and variability is calculated.

### 2.2.4 Turbidity Measurements

Absorbance at 600 nm was used to measure sample's turbidity. After High Pressure Homogenization, samples were subjected to measurements at four distinct time intervals: 1, 4, 7, and 24 hours, to monitor changes in turbidity over time. Before each turbidity measurement, samples were centrifuged at 10,000 rpm to separate the

supernatant, which was then used for absorbance reading. The absorbance at 600 nm (A600) was measured using a microplate reader (Allsheng, Hangzhou, China) which has a absorbance range from 0 to 4. According to Wu et al. (2019), A600 is a reliable indicator of the clarity or cloudiness of the solutions, with higher A600 values denoting increased turbidity. Each sample was analyzed in triplicate to ensure the precision and reproducibility of the results. This method facilitates a systematic evaluation of the impact of different protein concentrations and the presence of hydrocolloids on the turbidity of PPI solutions, providing a comprehensive understanding of the physicochemical properties of these formulations.

### 2.2.5 Particle Size measurements

Particle size distribution of solution was determined by laser light scattering using Mastersizer 3000 from Malvern Instruments Ltd. Considering the system contains pea protein isolate (PPI), which is a crucial factor in terms of stability, the relative index was set to 1.52 and the absorption parameter was set to 0.01 according to the study by He et al., (2024). Pea Protein Isolate size was evaluated using surface weighted average diameter D [3,2] and volume weighted average diameter D [4,3].

### 2.2.6 Statistical Analysis

Each experiment was repeated at least three times to ensure accuracy and consistency. For the purpose of statistical comparisons, one-way ANOVA and two-way ANOVA was used, setting the significance threshold at $p < 0.05$. The statistical software used for this analysis was MINITAB software, specifically Version 19.0. This software was important to interpret data for precision and reliability. The Tukey method was used for post-hoc comparison tests to determine significant differences between group means.

# CHAPTER 3

# RESULTS AND DISCUSSIONS

## 3.1 The testing of custom-build NMR probe on a model system

In this section, custom-built NMR probe which has been built was tested using a model food system. The effect of heating on the model system was investigated through a Total Soluble Solid (TSS) measurement and CPMG (Carr Purcell Meiboom Gill) $T_2^{eff}$ relaxometry. Then, a correlation has been made between them.

### 3.1.1 Total Soluble Solid (TSS) Content Measurements

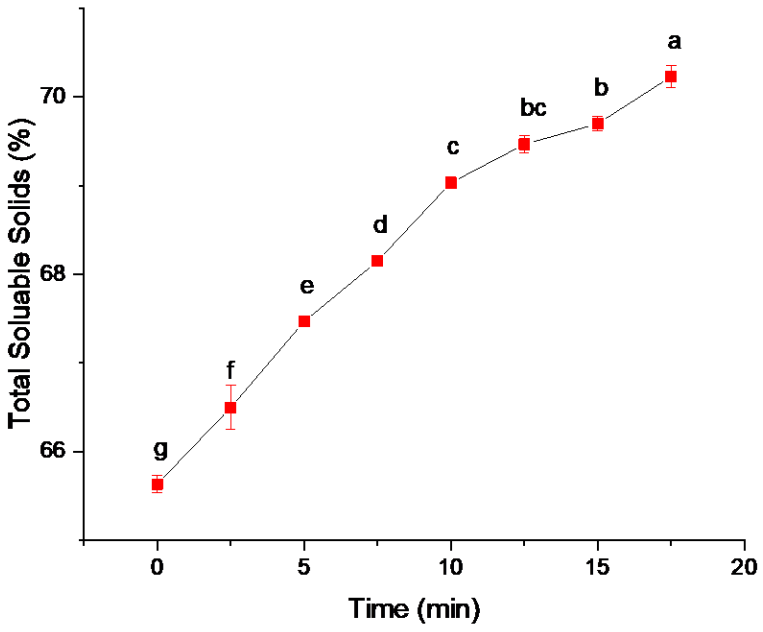


Figure 3.1 Heating time versus Total Soluble Solids (%Brix) is plotted.

Total Soluble Solids (TSS) is a critical quality parameter in food science. It is the concentration of dissolved solids in a solution. In this section, the relationship between heating time and TSS in a model food system composed of sucrose, corn syrup, gelatin, and water were examined. The TSS values were obtained using a refractometer (Hanna Instruments, Rhode Islands, USA) and plotted against different heating times as shown in Figure 3.1. As can be seen from this figure, there is a clear increasing trend over the plot. This is because of Figure 3.1 increasing heating time causes more moisture loss and more concentrated sample was obtained.

#### 3.1.1.1 CPMG ($T_2^{eff}$) Relaxation Results and correlation with Total Soluble Solids (TSS) content

In this part, $T_2$ relaxation times were correlated to Total Soluble Solid (TSS) in a model food system simulating the composition of a candy recipe. CPMG (Carr Purcell Meiboom Gill) $T_2^{eff}$ relaxation data (Figure 3.2) data collected during cooking periods were analyzed and their correlation to the TSS measurements was investigated.

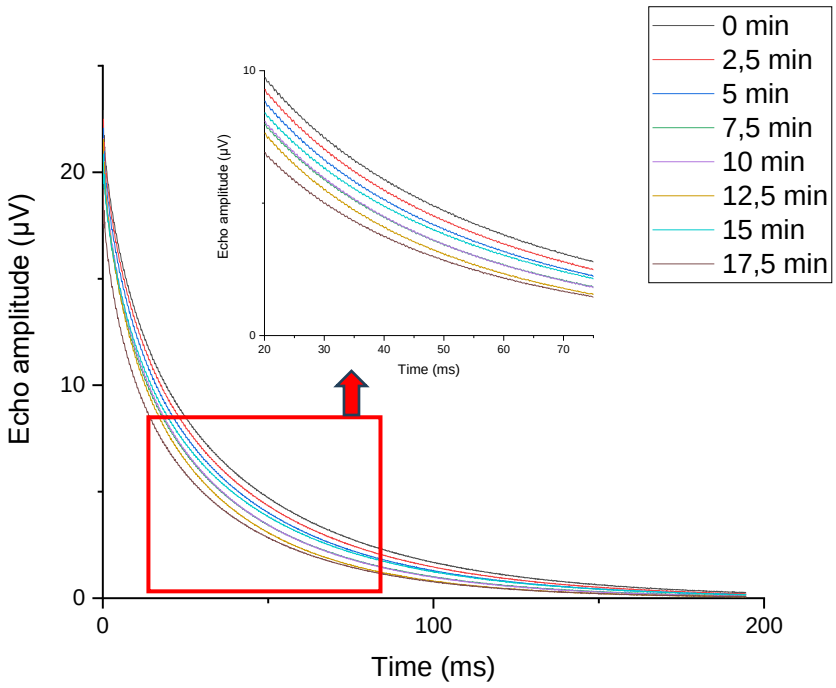


Figure 3.2 CPMG measurement taken for all samples

In the graph displayed in Figure 3.3, how the $T_2$ relaxation times change across cooking durations ranging from 0 to 17.5 minutes was observed. The graph illustrates a decline in $T_2$ relaxation times as the cooking progresses. This pattern is logical since longer cooking periods result in increased evaporation of water creating a denser and concentrated mixture with reduced free water content leading to lower $T_2$ relaxation times.

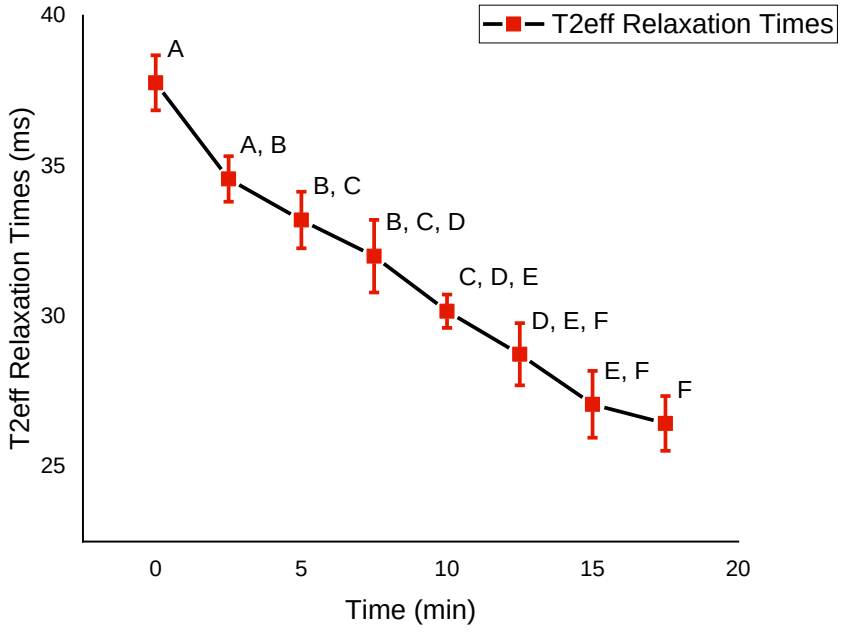


Figure 3.3 CPMG ($T_2^{eff}$) Relaxation Results vs Time

The main aim is to determine whether the Total Soluble Solids (TSS) content in the model food system could be accurately predicted using NMR relaxometry data. That's why, a regression analysis was conducted on the $T_2^{eff}$ relaxation times and TSS measurements. A linear pattern was observed on the plot of data and regression analysis was performed accordingly. The lack-of-fit test p-value is 0.210. This shows that there is no significant lack of fit and the model fits well. The high coefficient of determination ($R^2$ = 0.9113) shows that 91.13% of the variability in $T_2^{eff}$ can be attributed to heating time.

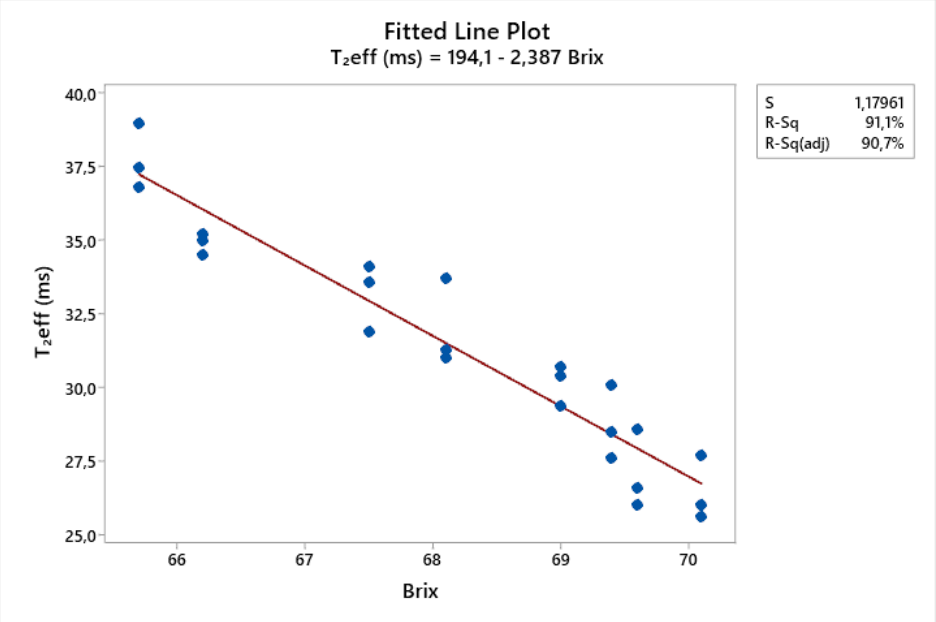


Figure 3.4 Linear regression analysis which performed to dataset.

$T_2^{eff}$ (ms) = 194,1 - 2,387 Time

The study results showed that combining NMR relaxometry with the analysis of $T_2^{eff}$ relaxation times offers a way to measure the Total Soluble Solids (TSS) content in a simulated food model. This method is effective in tracking changes in moisture levels and concentration while cooking. To make sure the use of this approach, it is essential to conduct validation studies across different types of foods and cooking conditions. Moreover, exploring sample varieties and cooking times will play a vital role in standardizing and improving the predictive accuracy of this NMR based technique. While Time-Domain Nuclear Magnetic Resonance (TD-NMR) techniques, such as Carr-Purcell-Meiboom-Gill (CPMG) sequences provide important information into the composition and properties of simple food systems, they are not always sufficient for more complex food structures.

The inherent limitations of NMR relaxometry in capturing detailed information and handling diverse matrices can limit its effectiveness in such scenarios. This constraint emphasizes the need to integrate imaging techniques, like Magnetic Resonance Imaging (MRI) as explored in the latter part of this research. MRI delivers spatial resolution and can map relaxation times throughout the sample providing a more comprehensive insight into complex food structures. It can increase capability to interpret the properties and behaviors of food systems under different processing conditions.

## 3.2 Uses of a Benchtop MRI system to investigate food stability through a model food system

To investigate the stability, traditional methods which are turbidity and particle size measurement, and novel 2D imaging methods are investigated using a model food system.

### 3.2.1 Turbidity

In this part, measurement aims to observe change in stability within the model food matrix which is pea protein isolate (PPI) solutions across a 24-hour period after high-pressure homogenization. The process starts with centrifuging each solution sample at designated time intervals (1, 4, 7, and 24 hours) and measuring the turbidity of the supernatant, demonstrating the removal of aggregated or precipitated proteins from the solution samples. The turbidity measurements were taken at 600 nm wavelength and showed on Table 3.1 and visually on Figure 3.5.

Table 3.1. Turbidity Measurements of PPI and HMP Mixtures at Different Concentrations and Time Intervals

| | %2 PPI and 0.5 HMP | %4 PPI and %0.5 HMP |
|---|---|---|
| Time (hours) | Absorbance (mean ± std) | Absorbance (mean ± std) |
| 1 | $0.873^{a} \pm 0.055$ | $1.761^{a} \pm 0.004$ |
| 4 | $0.739^{b} \pm 0.013$ | $1.586^{c} \pm 0.019$ |
| 7 | $0.663^{c} \pm 0.006$ | $1.675^{b} \pm 0.024$ |
| 24 | $0.561^{d} \pm 0.015$ | $1.553^{d} \pm 0.015$ |

***** Letters indicate statistically significant differences within each column, $p < 0.05$

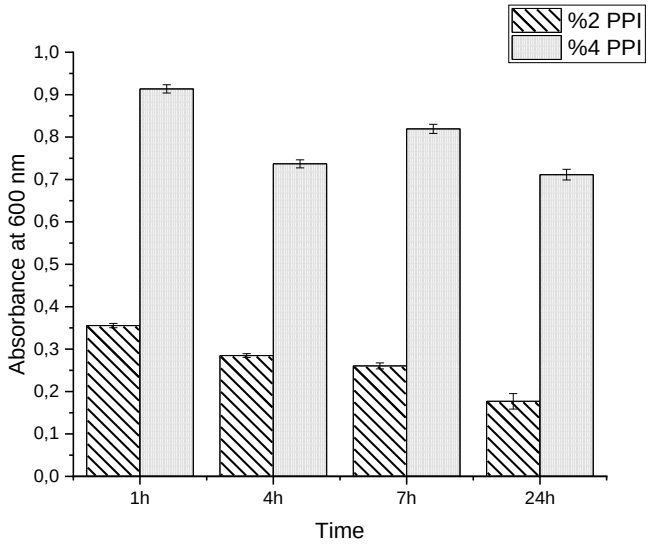


Figure 3.5 Turbidity Dynamics in 2% and 4% Pea Protein Isolate Solutions Over a 24-Hour Period

Measuring turbidity at 600 nm is important to determine the aggregation behavior of proteins in solutions, and turbidity measurements, often quantified by the absorbance at 600 nm, have been widely used to monitor protein aggregation processes (Dutta et al., 2015; McClements & Keogh, 1995; Utrera & Estévez, 2012). In a study by Jiang et al., (2010), heat-induced aggregation of soy protein isolates and its fractions

were analyzed using dynamic turbidity measurements at 600 nm. Similarly, in the research by Gbassi et al., (2012) turbidity was measured at 600 nm to analyze whey proteins in different environments.

Initially, the 2% PPI solution showed an absorbance of 0.873 ± 0.055 after 1 hour, whereas the 4% PPI solution displayed an initial absorbance/turbidity of 1.761 ± 0.004. In turbid solutions, depending on protein content, the absorbance increases linearly with protein concentration even in complex systems where proteins are bound to particles (Larson et al., 2018). The 2% solutions started with an initial absorbance of 0.873 ± 0.055 at the 1 hour reduced to 0.561 ± 0.015 at the 24 hours after HPH treatment and shown a significantly different decrease over time. The solutions with a 4% concentration displayed an initial absorbance of 1.761 ± 0.004. Then, reduced gradually to 1.553 ± 0.015 at the 24-hour. Other than the slight increase observed at the 7 hours for the 4% PPI solution, absorbance of all solution samples decreased over time. Collecting the supernatant for turbidity measurements after centrifugation at each time point removes the aggregated proteins from the model food system. This method isolates the clearer supernatant. Turbidity reduction reflects the extent of protein aggregation that has occurred and been removed by centrifugation. The decrease in turbidity over time for both concentrations is statistically significant ($p < 0.05$). These results showed that protein aggregation and sedimentation is happening over experiment duration of 24 hours.

### 3.2.2 Particle Size Measurement

The study of particle size distribution provides significant information of the aggregation behavior and stability of Pea Protein Isolate (PPI) solutions over time. This analysis is particularly related to understanding how protein concentration and time has influenced the formation and growth of aggregates in food systems. D [3,2] is a measure of the surface area-weighted mean diameter. Smaller particles size has stronger effect on the surface area-weighted mean diameter because they have higher

surface are to volume ratio. D [4,3], on the other hand, is a measure of the volume-weighted mean diameter.

Table 3.2. Light Scattering Particle Size Distribution Results

| | Time (hours) | D [3;2] | D [4;3] |
|---|---|---|---|
| **%2 PPI** | 1 | 1.433 ± 0.029 [d] | 5.367 ± 0.111 [e] |
| | 4 | 1.673 ± 0.015 [c] | 7.757 ± 0.140 [c] |
| | 7 | 2.557 ± 0.067 [b] | 8.407 ± 0.145 [b] |
| | 24 | 2.703 ± 0.032 [a] | 9.260 ± 0.061 [a] |
| **%4 PPI** | 1 | 0.702 ± 0.004 [f] | 3.363 ± 0.145 [g] |
| | 4 | 0.740 ± 0.008 [f] | 4.297 ± 0.095 [f] |
| | 7 | 0.770 ± 0.006 [f] | 5.347 ± 0.130 [d] |
| | 24 | 1.750 ± 0.010 [e] | 5.900 ± 0.030 [d] |

***** Letters indicate statistically significant differences within each column, $p < 0.05$

At 1 hour, the initial values show differences in the particle size results between the two concentrations. In the 2% PPI solution (as shown in Figure 3.2), peaks in the particle size distribution located at smaller size which is showing a well dispersed system with relatively small aggregates. The D [3,2] value is at 1.433 ± 0.029 μm, while the D [4,3] value is 5.367 ± 0.111 μm suggesting that most particles are small and evenly spread out (Table 3.2). As time passes, significant changes take place in the 2% PPI solution. At the 4 hours after HPH, there is a shift towards larger particle sizes with D [3,2] increasing to 1.673 ± 0.015 μm and D [4,3] reaching 7.757 ± 0.140 μm respectively. This pattern continues as D [3,2] rises to 2.557 ± 0.067 μm and D [4,3] rises to 8.407 ± 0.145 μm at the end of seven hours before increasing to values of approximately 2.703 ±.032 μm and 9.260±.061μm at 24 hours. The changes in particle sizes were found to be significant ($p < 0.05$). Aggregation led to an increase

in particle size shown by higher D [3,2] and D [4,3] values which is has a similar trend to studies by (Asen & Aluko, 2022; Munialo et al., 2014), as the protein aggregates grew in size. The 4% PPI solution (as shown in Figure 3.3) displays a different pattern in particle size distribution. After 1 hour, the solution exhibits a range of sizes with a peak at medium sizes. Initially, at 1 hour mark, The D [3,2] is 0.702 ± 0.004 µm and the D [4,3] is 3.363 ± 0.145 µm. As time progresses, the particle sizes in the 4% PPI solution also increases at a slower pace compared to the 2% solution. At 24 hours after HPH, D [3,2] increases significantly about to 1.750±.010µm. D [4,3] goes up to 5.900±.030µm ($p < .05$).

Similar to these results, Mession et al., (2012) demonstrated that pea protein dispersions showed significant aggregation and increase in particle size over time. Their study showed that protein molecules tend to aggregate more and resulting in larger particle sizes at that at higher concentrations and longer incubation periods.

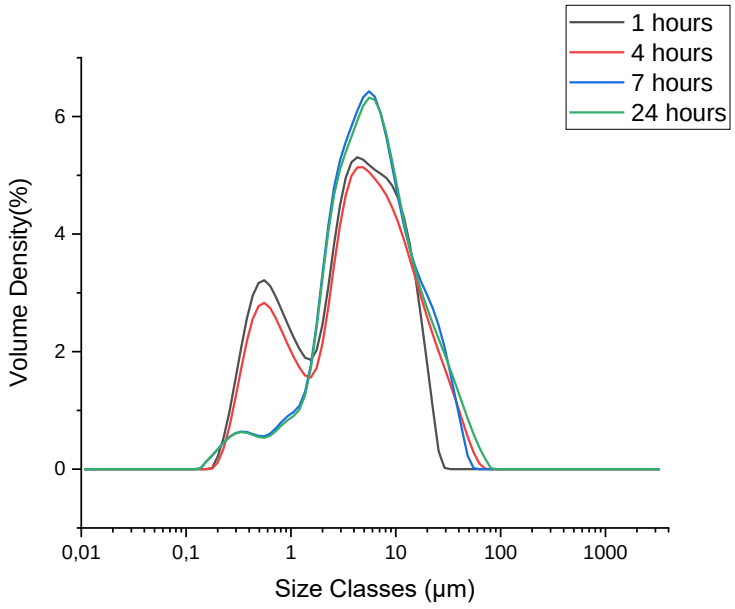


Figure 3.6 Particle distribution in 2% PPI containing solutions over a 24-Hour Period

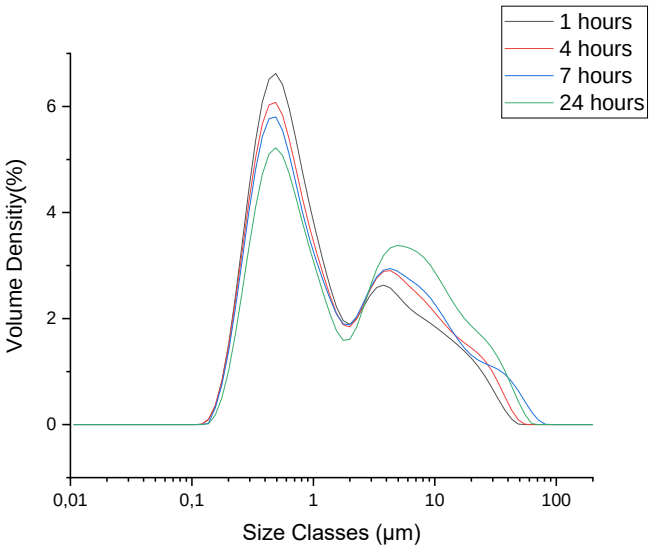


Figure 3.7 Particle distribution in 4% PPI containing solutions over a 24-Hour period

A study investigating the behavior of pea protein at various pH levels found that the protein tends to form larger aggregates when pH is near its isoelectric point (pI), (Krebs et al., 2007). pH of samples also measured in this thesis, and they are found to be pH of 5.99 for 2% PPI containing sample and pH of 6.44 4% PPI containing samples. Isoelectric points of pea protein isolates are around 4.9 (Lan et al., 2018b). This matches with the observation of larger initial D [3,2] and D [4,3] values in the 2% PPI solution.

### 3.2.3 2D Magnetic Resonance Imaging Analysis

In this section, effect of $MnCl_2$ is investigated in terms of shortening on $T_1$ relaxation time and showed its uses to shorten experiment time. Then, the stability and aggregation dynamics in solutions of pea protein isolate (PPI) and high-methoxyl pectin (HMP) after HPH was observed using $T_2$-weighted spin echo, using $T_1$-weighted spin echo, $T_2$ Mapping and $T_1$ Mapping pulse sequences to obtain 2D MR images over a 24-hour period.

### 3.2.3.1 Effect of $MnCl_2$

$MnCl_2$ is known as a $T_1$ contrast agent because of the paramagnetic properties (Kuo et al., 2005; Pautler et al., 1998). It shortens the $T_1$ relaxation times of protons. This shortening effect is due to the unpaired electrons in $Mn^{2+}$ ions since $Mn^{2+}$ ions generate a local magnetic field which has a strong effect on the nearby water protons.

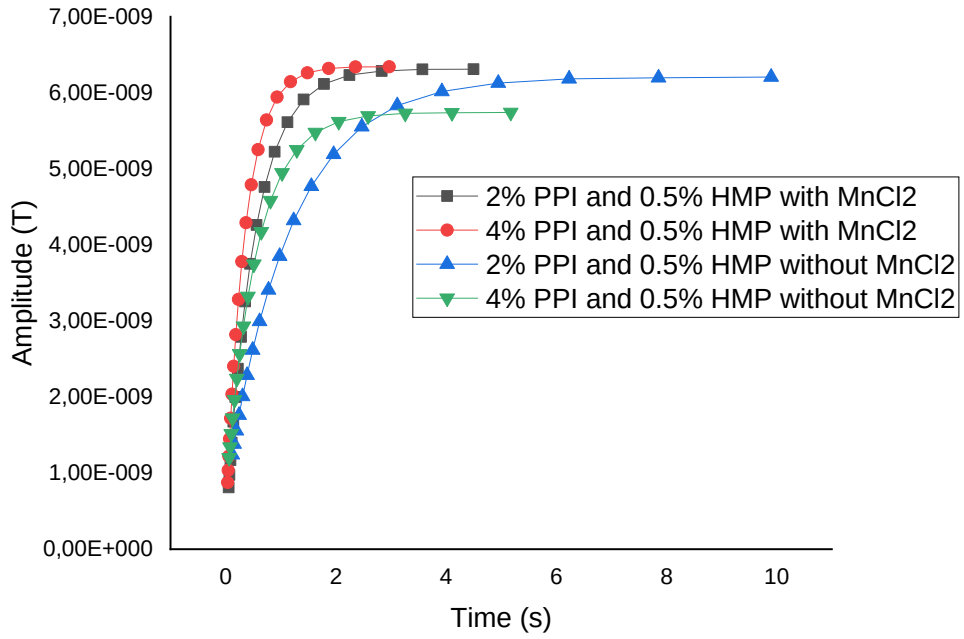


Figure 3.8 $T_1$ relaxation plots of solutions with $MnCl_2$ and without $MnCl_2$

The impact of manganese chloride ($MnCl_2$) on the $T_1$ relaxation times of Pea Protein Isolate (PPI) and High Methoxyl Pectin (HMP) mixtures is shown in Figure 3.8 which is showing $T_1$ relaxation plots for solutions with and without the addition of $MnCl_2$. In the solutions containing $MnCl_2$ (represented by black squares for 2% PPI and red circles for 4% PPI), the $T_1$ relaxation times are shorter, and this can be observed through slopes of the relaxation curves since it is rapidly approaching to the equilibrium. $MnCl_2$'s role as a $T_1$ contrast agent in the PPI and HMP mixtures for

decreasing $T_1$ relaxation time is clearly demonstrated, and new relaxation rates provided faster imaging and greater contrast in MRI applications.

#### 3.2.3.2 $T_2$-Weighted 2D Spin Echo Images

The structural changes and aggregation dynamics in solutions of pea protein isolate (PPI) and high-methoxyl pectin (HMP) was examined after HPH using $T_2$-weighted spin echo MRI imaging over a 24-hour period. Representative $T_2$-weighted MRI images of the PPI-HMP mixtures at different concentrations and time intervals are shown in Figure 3.11 to Figure 3.13. These images are presented in a color scale shown in 3.10 where red indicates higher signal intensity than blue. Initially, all samples exhibited relatively high signal intensity, reflecting their initial water content and the homogenous distribution of particles. As time progressed, changes in signal intensity were observed, correlating with the formation and growth of aggregates. First, to understand MRI images shown in figures, one needs to understand the mechanism behind it and needs to know what the colors (red, blue, yellow) represent. The changes in signal intensity in $T_2$-weighted images can be explained by the variations in $T_2$ relaxation times. The $T_2$ relaxation time reflects how quickly protons in the sample lose phase coherence due to local magnetic field inhomogeneities.

Figure 3.9. Colormap “jet”

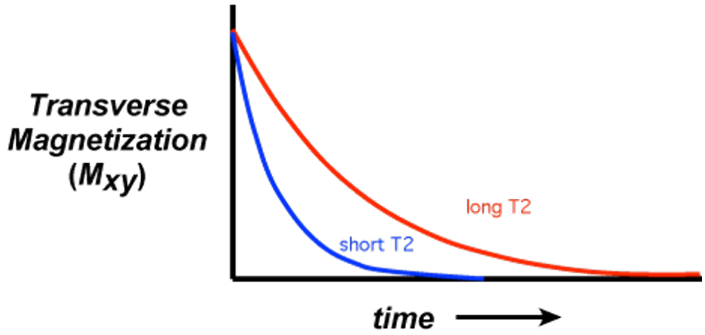


Figure 3.10 Comparison of Longitudinal Magnetization Recovery Curves for Short and Long $T_1$ Times

$$M_t = M_{max} * e^{-t/T_2} \quad (1)$$

where:

- $M_t$ is the magnetization at time t.
- $M_{max}$ is the maximum magnetization at the beginning.
- $T_2$ is the $T_2$ relaxation time.
- t is the time after the RF pulse.

For regions with long $T_2$ relaxation times, the term $e^{-t/T2}$ decreases slowly compared to regions with short $T_2$ relaxation times. As a result, $M_t$ stays relatively high over a longer period, resulting in higher magnetization and eventually higher signal intensity in $T_2$ weighted images. For the regions with short $T_2$, the term $e^{-t/T_2}$ rapidly decreases towards zero. Consequently, $M_t$ diminishes quickly, resulting in lower magnetization. This leads to lower signal intensity in $T_2$ weighted images.

The $T_2$-weighted MRI images in Figures 3.11 to 3.13 are displayed using a "jet" colormap (Figure 3.9), which is a common color scale in MRI imaging. In this colormap, colors range from blue to red, representing different levels of signal intensity.

This color coding helps visualize the distribution of water and the structural changes within the samples. Brighter colors (yellow to red) suggest areas with higher proton mobility, indicative of liquid or less dense aggregates. Darker colors (blue) indicate areas with lower proton mobility.

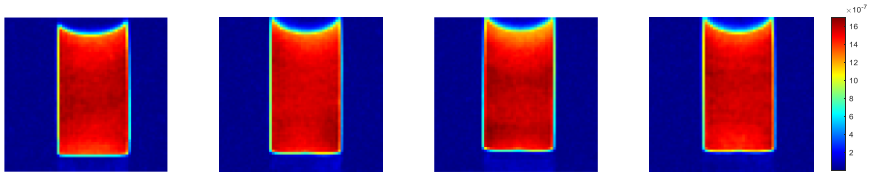

Figure 3.11. $T_2$ weighted Spin Echo images of control group (no protein) model food system over 24 Hours

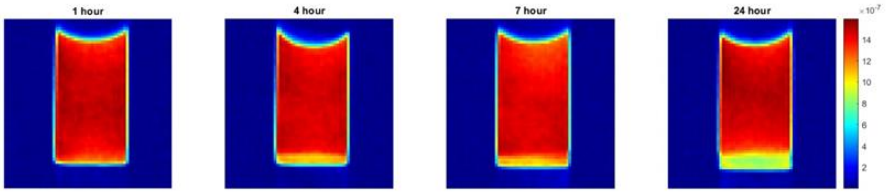


Figure 3.12. $T_2$ weighted Spin Echo Images of 2% pea protein isolate model food system Over 24 Hours

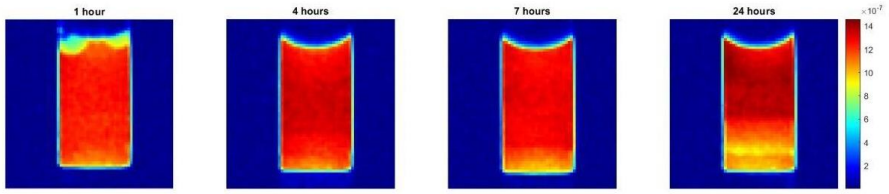


Figure 3.13 $T_2$ weighted Spin Echo images of 4% pea protein isolate model food system over 24 Hours

Figure 3.11 displays the $T_2$ weighted spin echo MRI scans of the control sample throughout the 24-hour timeframe. The signal intensity stayed consistent and steady suggesting that no changes in the internal composition or water mobility of the mixture. This uniformity implies that there was no aggregation or settling as expected in the control sample lacking PPI. Statistical analysis further confirms this stability by revealing no significant differences in $T_2$ signal intensity over time ($p > 0.05$) emphasizing the consistency and structural integrity of the control sample (Table 3.3). Conversely, Figure 3.12 illustrates the $T_2$ images for the mixture containing 2% PPI. Initially at 1 hour a uniform high signal intensity with contrast was observed in the image. However, as duration over 24 hours a significant decrease in signal intensity took place towards the bottom of the sample. The statistical analysis indicated significant differences in signal intensity over the 24-hour period ($p < 0.05$).

The observed trend in signal intensity, with darker regions at the bottom, reflects the increasing aggregation of particles as they settle. 4% PPI containing sample was also similar. The signal intensity at 4% PPI initially Figure 3.13, shows a dispersed solution. Over a 24-hour period there was a decrease in signal intensity especially in the lower regions suggesting the formation of dense aggregates leading to quick proton dephasing. These protein aggregates can restrict water molecule movement by creating a network resulting in shorter $T_2$ relaxation times. The reduction in $T_2$ relaxation times varies depending on the size and type of protein aggregates with larger aggregates which is limiting the water mobility (Indrawati et al., 2007). Table 3.3 shows differences in signal intensity over the 24-hour period ($p < 0.05$) indicating the rapid formation and sedimentation of large aggregates ultimately causing shorter $T_2$ relaxation times and lower signal intensities. The decrease in $T_2$ weighted image signal intensity was observed in both 2% and 4% PPI solutions. Results are consistent with K. P. Wu & Baum (2010) that protein aggregation leads to shorter $T_2$ relaxation times due to enhanced dipolar−dipolar interactions among protein protons. These interactions delay the rotational motion that typically averages out such effects. Thus, it reduces the $T_2$ relaxation times and signal intensity.

Table 3.3 Results of $T_2$ weighted Spin Echo images of protein isolate model food system over 24 hours

| | Time(hours) | Intensity Mean ± Error | Std Mean ± Error |
|---|---|---|---|
| **Control Sample** | 1 | $1.559 \pm 0.026^{a}$ | $0.037 \pm 0.019$ |
| | 4 | $1.563 \pm 0.001^{a}$ | $0.030 \pm 0.005$ |
| | 7 | $1.572 \pm 0.018^{a}$ | $0.035 \pm 0.005$ |
| | 24 | $1.556 \pm 0.010^{a}$ | $0.041 \pm 0.018$ |
| **%2 PPI** | 1 | $1.424^{b} \pm 0.025^{b}$ | $0.066 \pm 0.006$ |
| | 4 | $1.403^{bc} \pm 0.014^{bc}$ | $0.099 \pm 0.019$ |
| | 7 | $1.367^{c} \pm 0.011^{c}$ | $0.106 \pm 0.002$ |
| | 24 | $1.294^{d} \pm 0.017^{d}$ | $0.228 \pm 0.026$ |
| **%4 PPI** | 1 | $1.224^{d} \pm 0.009^{d}$ | $0.025 \pm 0.013$ |
| | 4 | $1.285^{de} \pm 0.012^{de}$ | $0.045 \pm 0.007$ |
| | 7 | $1.251^{e} \pm 0.015^{e}$ | $0.057 \pm 0.005$ |
| | 24 | $1.161^{f} \pm 0.003^{f}$ | $0.105 \pm 0.034$ |

*Letters indicate statistically significant differences within each column, $p < 0.05$

It is important to note that, standard deviation ($4^{th}$ column) shown in Table 3.3 does not show deviation over the image replicates, but the deviation over the intensity values of voxels in the 2D images. Standard deviation itself can be an important parameter to observe the stability as inhomogeneous regions will result in higher standard deviations. The control sample, as expected, is constant over 24h duration. However, 2% and 4% PPI containing samples' standard deviation is increasing from 0.066 to 0.228 for 2% PPI and 0.025 to 0.105 for 4% PPI. It is clear that aggregation occurring over time resulted in inhomogeneities in the inspected region ROI.

### 3.2.3.3 $T_1$-Weighted 2D Spin Echo Images

The differentiation in color between the bottom and top regions in the $T_1$ weighted images is important for understanding the internal dynamics of these mixtures. Moving to the $T_1$ weighted imaging, there are visual differences. For example, considering Figure 3.17 and Figure 3.12 (a single slice drawn side by side in Figure 3.14 for ease of comparison) which has different weighting applied over same sample, red regions appear on $T_2$ weighted appear yellow with $T_1$ weighting which indicates low intensity for that region.

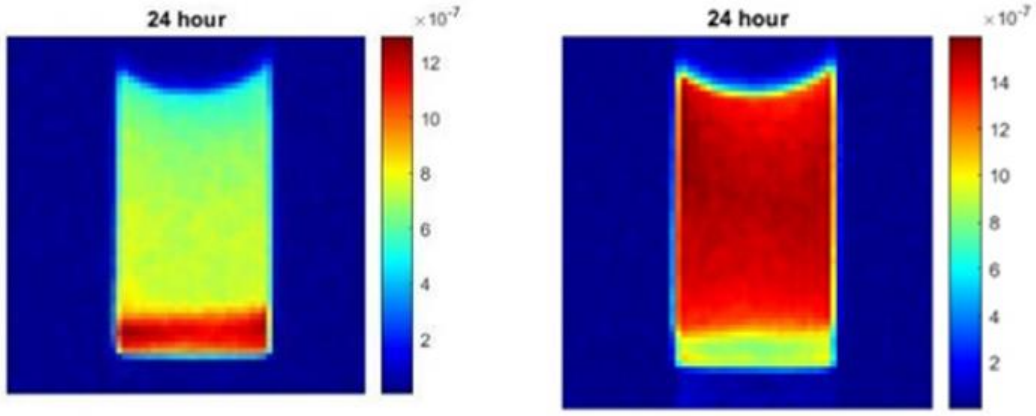


Figure 3.14 Comparison between $T_1$(on left) and $T_2$(on right) weighted images

In $T_1$ weighted imaging, the intensity of the signal is influenced by the $T_1$ relaxation time. which is the time it takes for protons in tissues to realign with the external magnetic field (Figure 3.15). Regions with short $T_1$ relation time, resulted in a higher signal intensity on $T_1$ weighted images (Bernstein et al., 2004) corresponding to the changes in density of the aggregates.

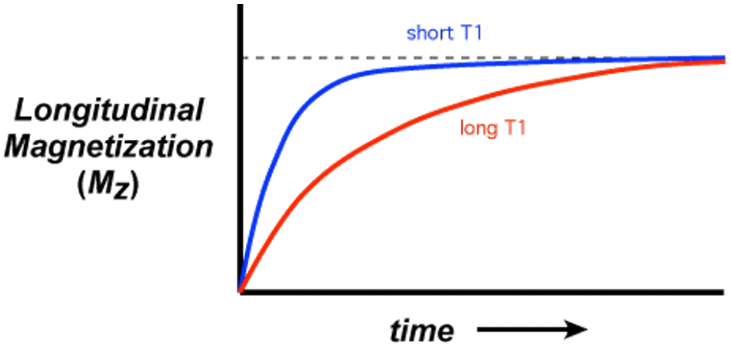


Figure 3.15 Comparison of longitudinal magnetization recovery curves for short and long $T_1$ times

$$M_t = M_{max} * (1 - e^{-t/T_1}) \quad (2)$$

where:

- $M_t$ is the magnetization at time t.
- $M_{max}$ is the maximum equilibrium magnetization.
- $T_1$ is the $T_1$ relaxation time.
- t is the time after the RF pulse.

As shown in Equation 2, in regions with short $T_1$ relaxation times, the recovery of magnetization occurs quickly. Because short $T_1$ will cause term $e^{-t/T_1}$ rapidly approach zero and result in Mt approaching $M_{max}$. Therefore, at any given time t, $M_t$ is close to $M_{max}$, yielding high magnetization. On the other hand, in regions with long $T_1$ relaxation times, long $T_1$ leads to, the term $e^{-t/T1}$ becoming significantly larger for a longer duration, causing Mt to increase more slowly to $M_{max}$. Therefore, $M_t$ remains lower compared to $M_{max}$ for the same t giving lower magnetization.

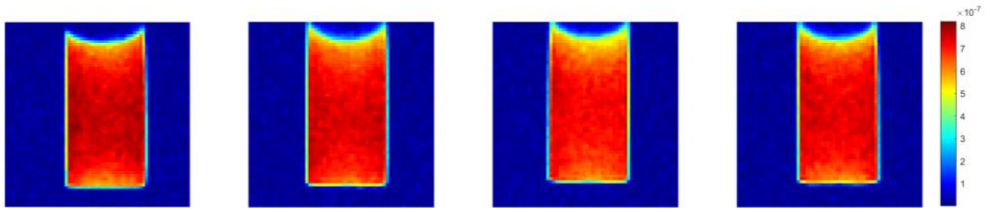

Figure 3.16. $T_1$ weighted Spin Echo images of control group isolate model food system over 24 Hours

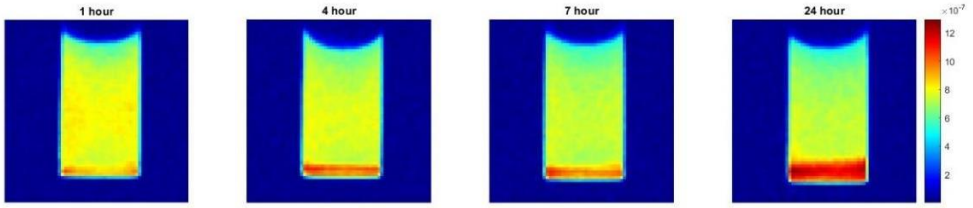


Figure 3.17. $T_1$ weighted Spin Echo images of 2% pea protein isolate model food system over 24 Hours

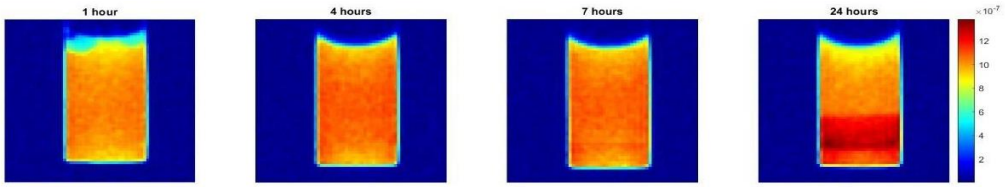


Figure 3.18 $T_1$ weighted Spin Echo images of 4% pea protein isolate Model Food System Over 24 Hours

Figure 3.16 displays the $T_1$ weighted spin echo MRI scans of the control sample (no protein) over a 24-hour period. The images show a stable signal intensity throughout the observation time indicating a stable water distribution and no significant aggregation (Table 3.4). The average signal intensity remains steady at around 0.733 ± 0.012 at 1 hour and 0.732 ± 0.002 at 24 hours. Results are not significantly different over time showing that stability in $T_1$ weighted signal intensity over time ($p > 0.05$). In the case of the 2% PPI mixture, there are significant changes in $T_1$ weighted images are observed over the duration as shown in Figure 3.17. Initially, the images

show signal intensity with an average value of 0.788 ± 0.008 at one hour. Over time, the signal intensity rises to 0.868±0.023 after 24 hours. The designated ROI area in the regions reveals that as aggregates form there is an increase, in signal intensity which may be associated with enhanced local magnetic fields and shortened $T_1$ relaxation times.

This change is even statistically significant ($p < 0.05$). Like the 2% PPI mixture, Figure 3.18 shows the $T_1$ weighted MRI images of the 4% PPI mixture. Initially the mixture displayed a signal intensity averaging at 0.762 ± 0.012 after 1 hour similar suggesting a uniform dispersion. However, over time the signal intensity rose to 1.183 ± 0.019 after 24 hours in the lower areas. The results showed that variations in $T_1$ signal intensity, throughout the 24-hour period ($p < 0.05$) indicating accelerated aggregation and settling processes in the 4% PPI solution.

Table 3.4 Results of $T_1$ weighted Spin Echo images of protein isolate model food system over 24 hours

| | **Time(hours)** | **Intensity Mean ± Error** | **Std Mean ± Error** |
|---|---|---|---|
| **Control Sample** | 1 | $0.733^{fg} \pm 0.012$ | 0.020 ± 0.001 |
| | 4 | $0.736^{g} \pm 0.016$ | 0.020 ± 0.003 |
| | 7 | $0.736^{g} \pm 0.021$ | 0.021 ± 0.001 |
| | 24 | $0.732^{g} \pm 0.002$ | 0.019 ± 0.003 |
| **%2 PPI** | 1 | $0.788^{def} \pm 0.008$ | 0.065 ± 0.030 |
| | 4 | $0.791^{de} \pm 0.006$ | 0.086 ± 0.011 |
| | 7 | $0.804^{d} \pm 0.011$ | 0.145 ± 0.059 |
| | 24 | $0.868^{c} \pm 0.023$ | 0.176 ± 0.013 |
| **%4 PPI** | 1 | $0.762^{efg} \pm 0.012$ | 0.107 ± 0.136 |
| | 4 | $1.081^{b} \pm 0.012$ | 0.033 ± 0.005 |
| | 7 | $1.065^{b} \pm 0.002$ | 0.029 ± 0.005 |
| | 24 | $1.183^{a} \pm 0.019$ | 0.089 ± 0.014 |

**letters indicate statistically significant differences within each column, $p < 0.05$*

### 3.2.3.4 $T_1$ Mapping

Figure 3.19 and Figure 3.20 are representative for $T_1$ maps of different concentrations of Pea Protein Isolates and durations after HPH treatment at 500 MPa. Each voxel in these images carries the information of $T_1$ relaxation time specifically to the designated location. Resolution of these images are 48x48. In $T_1$ Mapping images, contrast generated by $T_1$ relaxation times difference among the voxel in an image. The $T_1$ relaxation time is influenced by the mobility and interaction of water molecules within the sample. Voxel with high proton mobility, high water content will be going to have longer areas with dense aggregates or reduced water mobility show shorter $T_1$ relaxation times.

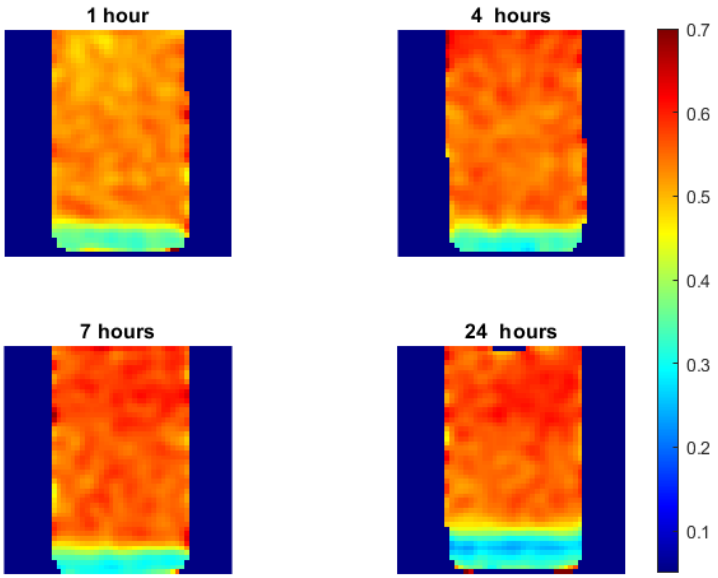


Figure 3.19 $T_1$ Mapping of 2% Pea Protein Isolate (PPI) Solution Over 24 Hours.

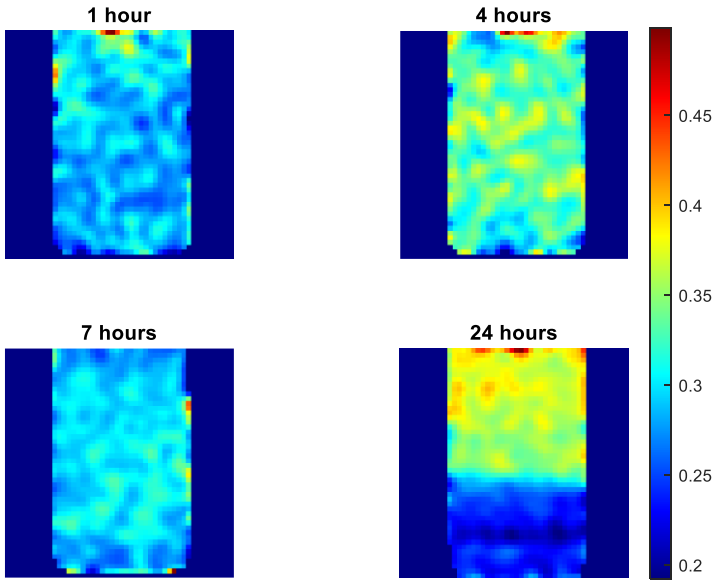


Figure 3.20 $T_1$ Mapping of 4% Pea Protein Isolate (PPI) Solution Over 24 Hours.

At 1 hour, both solutions (top-left images in Figure 3.19 and Figure 3.20) shows high $T_1$ relaxation times. This uniformity in the distribution of $T_1$ relaxation time values is because of the presence of largely free water molecules within the protein matrix. The 2% PPI solution displays slightly higher $T_1$ values compared to the 4% PPI solution, indicating more free water or less densely packed protein molecules in the less concentrated solution. By 24 hours (bottom-right images in Figure 3.19 and Figure 3.20), both solutions show lower $T_1$ relaxation time values in the lower regions of the samples. The corresponding histograms (Figure 3.21 and Figure 3.22) quantify these observations. Initially, at 1 hour, 2% PPI solution had a peak $T_1$ distribution around 0.55 while 4% PPI solutions peak was located at 0.33. This is consistent with the presence of free water. The peaks shifted towards lower $T_1$ values over time such that the 4% PPI solution at 24 hours demonstrate a dual peak structure, with one peak around 0.2 seconds and another at approximately 0.35 seconds. This also shows inhomogeneity through the sample.

When proteins unfold, their inner hydrophobic parts are exposed, causing them to clump together due to hydrophobic forces. This results in the formation of protein structures that are held together by these forces, shielding them from water and limiting their movement (Saio et al., 2014). Aggregating proteins into shapes, such as shifting from a random coil to a helical structure and forming tetramers, can greatly slow the movement of water around these aggregates (Qiu et al., 2005). Having hydrophobic surfaces can speed up the unfolding and aggregation of proteins and has an effect on how freely water molecules can move. (March et al., 2021). So, similar to the trend in $T_1$ Mapping results from the images, $T_1$ should be smaller when aggregation happening due to decrease in water mobility.

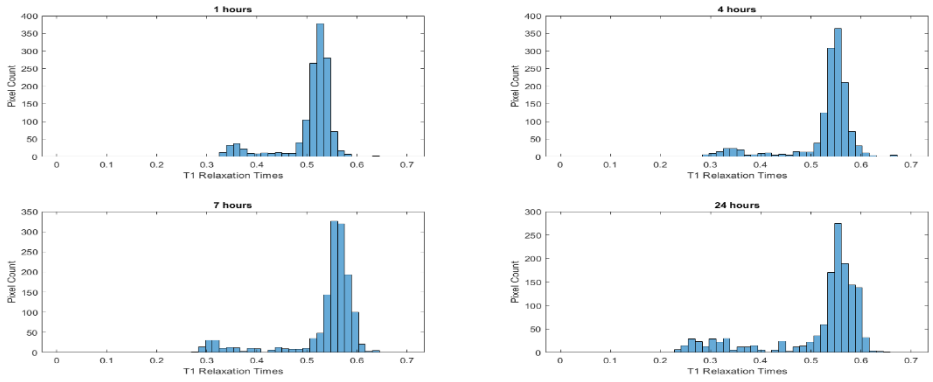


Figure 3.21 Histogram $T_1$ Distribution through the image (2%)

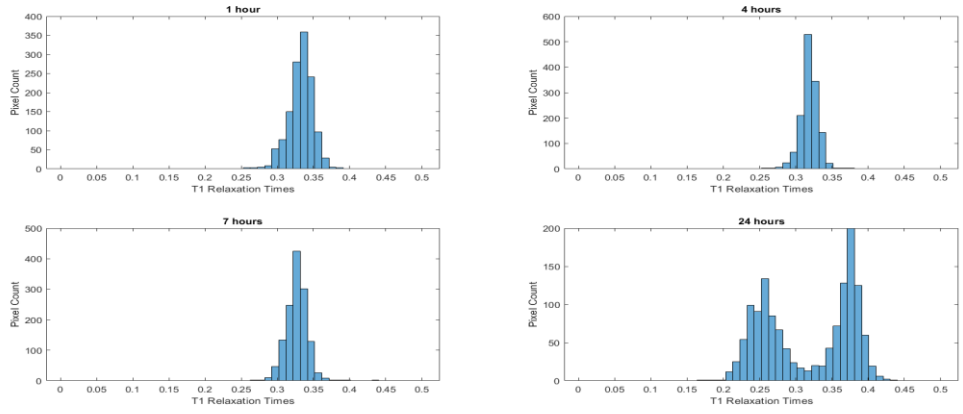


Figure 3.22 Histogram $T_1$ Distribution through the image (4%)

### 3.2.3.5 $T_2$ Mapping

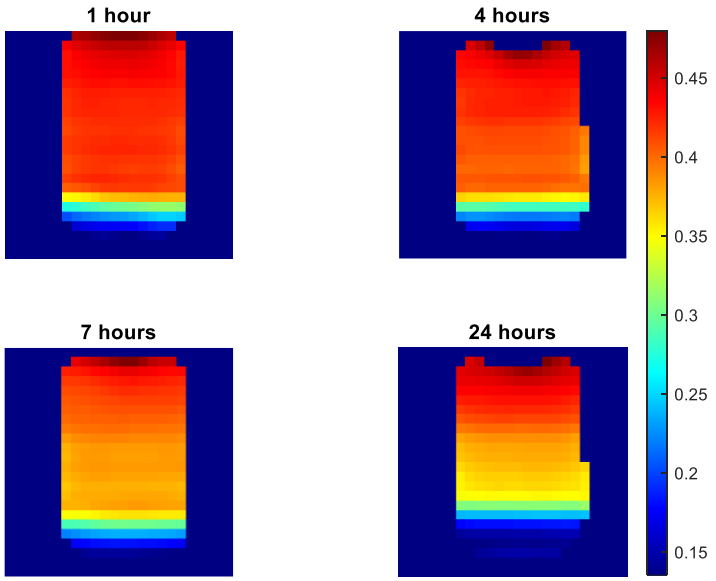


Figure 3.23 $T_2$ Mapping of 2% pea protein isolate (PPI) solution over 24 Hours

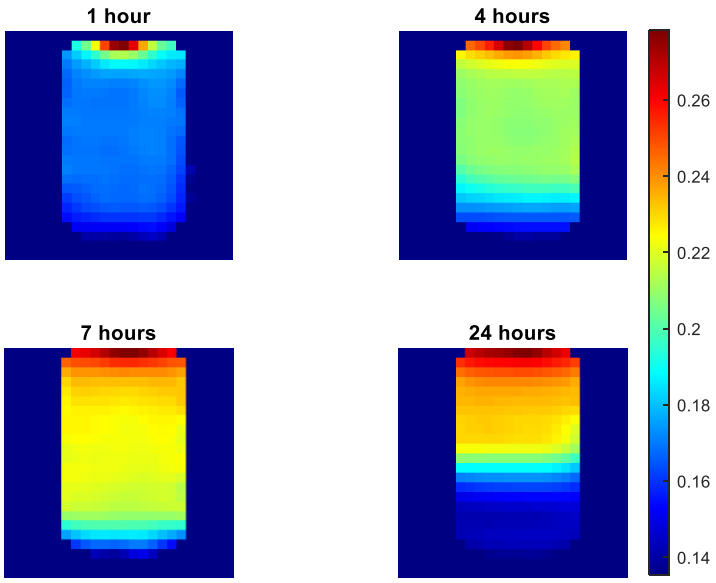


Figure 3.24 $T_2$ Mapping of 4% pea protein isolate (PPI) solution over 24 Hours

The top-left images in Figure 3.23 and Figure 3.24 shows the $T_2$ maps for the 2% and 4% PPI solutions 1, 4, 7, and 24 hours after HPH treatment, respectively. Each voxel in these images represents the local $T_2$ relaxation time and the resolution set at 24x24 pixels. The color contrast in these maps is generated by differences in $T_2$ relaxation times. High $T_2$ relaxation times are shown by the dominance of red and orange regions. Initially, the $T_2$ maps show a uniform distribution of relaxation times with higher $T_2$ values. However, as time progresses, distinct regions of varying $T_2$ values become apparent.

The 2% PPI solution found to be show higher $T_2$ values compared to the 4% PPI solution because of more free water available. At higher concentration, more protein will bound the water and leads to a lower water mobility. At such cases, $T_2$ relaxation times decreases which is shown study by (Szuminska et al., 2001).

The histograms in Figure 3.25 and Figure 3.26 provide a quantitative perspective on the distribution of $T_2$ relaxation times in the 2% and 4% PPI solutions over 24-hour duration period. In the case of the 2% PPI solution, the histograms display a relatively narrow distribution of $T_2$ values around 0.45 at the beginning and decreases to 0.15 to 0.2 seconds.

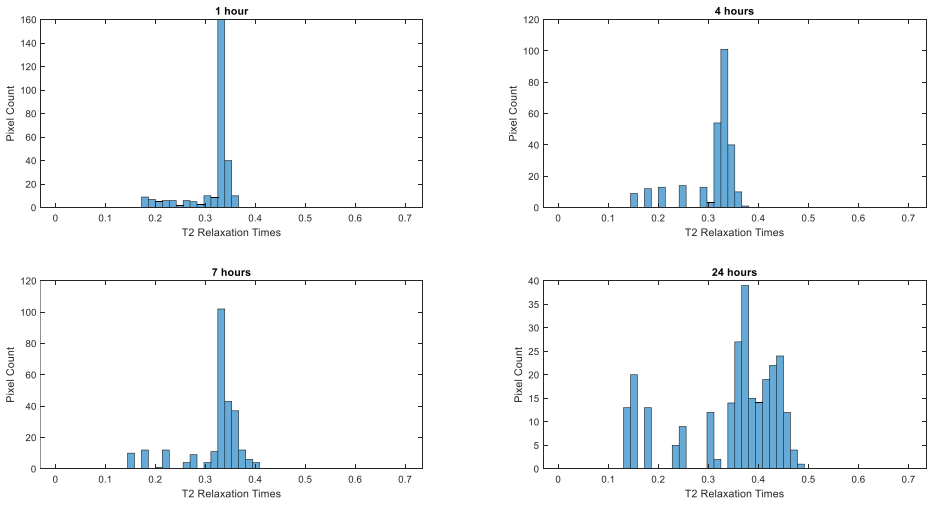


Figure 3.25 Histogram $T_2$ distribution through the image (2%)

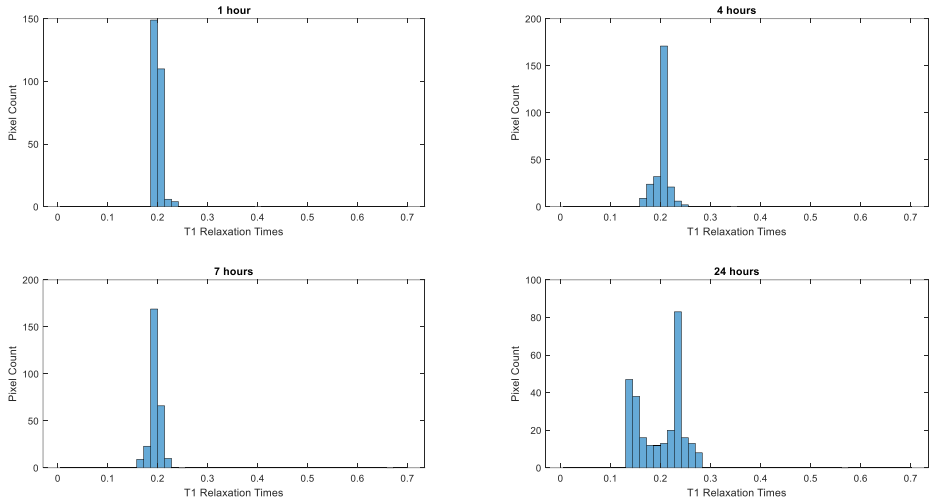


Figure 3.26 Histogram $T_2$ distribution through the image (4%)

# CHAPTER 4

## CONCLUSION & RECOMMENDATIONS

Food stability has always been the interest of the consumers, food producers and regulatory authorities. It is becoming more significant due to the food safety and food quality issues. In this thesis, the initial part of the study focused on the development and optimization of a portable NMR probe which will be used to analyze food systems stability. This probe first used a Halbach array magnet setup to create a uniform magnetic field, which is critical for accurate NMR measurements. The design process included simulations to optimize the magnetic field homogeneity and strength, ensuring reliable readings of the sample properties. Then, this custom-built portable NMR probe was tested through a model food system which consists of sucrose, corn syrup, gelatine and water. Correlations done through a linear regression model confirmed its use to monitor the Total Soluble Solids (TSS) Content and correlated it with $T_2^{eff}$ relaxation times. To determine if imaging is necessary to fully understand complex food systems, a benchtop Magnetic Resonance Imaging (MRI) was used to assess the food stability in a model food system which is focusing on pea protein isolate (PPI) mixed with high methoxyl pectin (HMP). The particle size measurements demonstrated that surface weighted average diameter D [3,2] and volume weighted average diameter D [4,3] are increasing over the duration. 2% PPI containing samples particle sizes are higher than 4% PPI containing ones because of pH of 2% PPI containing samples is closer to isoelectric point. Both $T_1$ and $T_2$ weighted spin echo imaging provide a good contrast based on the images and the quantification of the images was significantly different ($p<0,05$). These images allowed for the observation of changes in the distribution and concentration of PPI aggregates over time which correlates with stability. On the other hand, $T_1$ and $T_2$ Mapping, localized $T_1$ and $T_2$ relaxation times in different regions on the sample. As PPI aggregates, distribution and visibility of

aggregates become evident in the MRI images. Over time, regions with dense aggregates demonstrated significantly different lower signal intensities in $T_2$-weighted images and shorter $T_2$ relaxation times due to water mobility and protein-protein interactions ($p<0,05$). On the other hand, $T_1$ weighted images had significantly higher intensities due shorter $T_1$ relaxation times in these regions ($p<0,05$). The heterogeneity of the sample in the vertical dimension suggests that at least one imaging dimension is needed to fully monitor the properties of such model food systems.

As a future improvement to the custom built Halbach magnet could be adding a new dimension (addition of gradient into z-direction), then the system can evolve into a 1D profiler which will allow spatial measurements along an axis. Then, it will be possible to collect information on homogeneity and stability of the sample where NMR relaxometry is lacking. The MRI measurements used in the second part can then be performed through a low-cost benchtop Halbach magnet. For the 2D imaging applications, extending it to broader food matrices such as emulsion, gels can confirm the methods effectiveness. Also, MRI results should be correlated with more analytical techniques, such as Differential Scanning Calorimetry.

## REFERENCES


Aboonajmi, M., & Faridi, H. (2016). *Nondestructive quality assessment of Agro-food products*. www.cfb.unh.edu

Ahern, N., Arendt, E. K., & Sahin, A. W. (2023). Protein Soft Drinks: A Retail Market Analysis and Selected Product Characterization. *Beverages*, *9*(3). https://doi.org/10.3390/beverages9030073

Asen, N. D., & Aluko, R. E. (2022). Physicochemical and Functional Properties of Membrane-Fractionated Heat-Induced Pea Protein Aggregates. *Frontiers in Nutrition*, *9*, 852225. https://doi.org/10.3389/FNUT.2022.852225/BIBTEX

Asioli, D., Aschemann-Witzel, J., Caputo, V., Vecchio, R., Annunziata, A., Næs, T., & Varela, P. (2017). Making sense of the "clean label" trends: A review of consumer food choice behavior and discussion of industry implications. In *Food Research International* (Vol. 99, pp. 58–71). Elsevier Ltd. https://doi.org/10.1016/j.foodres.2017.07.022

Bernstein, M. A., King, K. F., & Zhou, X. J. (2004). Handbook of MRI Pulse Sequences. *Handbook of MRI Pulse Sequences*, 1–1017. https://doi.org/10.1016/B978-0-12-092861-3.X5000-6

Blümich, B. (2019). Low-field and benchtop NMR. *Journal of Magnetic Resonance*, *306*, 27–35. https://doi.org/10.1016/j.jmr.2019.07.030

Blümich, B., Anferov, V., Anferova, S., Klein, M., Fechete, R., Adams, M., & Casanova, F. (2002). Simple NMR-MOUSE with a bar magnet. *Concepts in Magnetic Resonance Part B: Magnetic Resonance Engineering*, *15*(4), 255–261. https://doi.org/10.1002/cmr.10046

Casanova, F., Perlo, J., & Blümich, B. (2011). Single-sided NMR. *Single-Sided NMR*, 1–244. https://doi.org/10.1007/978-3-642-16307-4/COVER

Chavhan, G. B., Babyn, P. S., Thomas, B., Shroff, M. M., & Mark Haacke, E. (2009). Principles, Techniques, and Applications of T2*-based MR Imaging and Its Special Applications. *Radiographics*, *29*(5), 1433. https://doi.org/10.1148/RG.295095034

Desrumaux, A., & Marcand, J. (2002). Formation of sunflower oil emulsions stabilized by whey proteins with high-pressure homogenization (up to 350 MPa): effect of pressure on emulsion characteristics. *International Journal of Food Science and Technology*, *37*(3), 263–269. https://doi.org/10.1046/J.1365-2621.2002.00565.X

Dutta, C., Yang, M., Long, F., Shahbazian-Yassar, R., & Tiwari, A. (2015). Preformed Seeds Modulate Native Insulin Aggregation Kinetics. *The Journal of Physical Chemistry. B*, *119*(49), 15089–15099. https://doi.org/10.1021/ACS.JPCB.5B07221

Gan, Z., Kwak, H. T., Bird, M., Cross, T., Gor'kov, P., Brey, W., & Shetty, K. (2008). High-field NMR using resistive and hybrid magnets. *Journal of Magnetic Resonance*, *191*(1), 135–140. https://doi.org/10.1016/j.jmr.2007.12.008

Gbassi, G., Yolou, F., Sarr, S., Atheba, P., Amin, C., & Ake, M. (2012). Whey proteins analysis in aqueous medium and in artificial gastric and intestinal fluids. *International Journal of Biological and Chemical Sciences*, *6*(4). https://doi.org/10.4314/IJBCS.V6I4.38

Giovannetti, G., Fontana, N., Flori, A., Santarelli, M. F., Tucci, M., Positano, V., Barmada, S., & Frijia, F. (2024). Machine Learning for the Design and the Simulation of Radiofrequency Magnetic Resonance Coils: Literature Review, Challenges, and Perspectives. In *Sensors* (Vol. 24, Issue 6). Multidisciplinary Digital Publishing Institute (MDPI). https://doi.org/10.3390/s24061954

Grote, U., Fasse, A., Nguyen, T. T., & Erenstein, O. (2021). Food Security and the Dynamics of Wheat and Maize Value Chains in Africa and Asia. In *Frontiers*

*in Sustainable Food Systems* (Vol. 4). Frontiers Media S.A. https://doi.org/10.3389/fsufs.2020.617009

Gruber, B., Froeling, M., Leiner, T., & Klomp, D. W. J. (2018). RF coils: A practical guide for nonphysicists. In *Journal of Magnetic Resonance Imaging* (Vol. 48, Issue 3, pp. 590–604). John Wiley and Sons Inc. https://doi.org/10.1002/jmri.26187

Guo, Z., Huang, Z., Guo, Y., Li, B., Yu, W., Zhou, L., Jiang, L., Teng, F., & Wang, Z. (2021). Effects of high-pressure homogenization on structural and emulsifying properties of thermally soluble aggregated kidney bean (Phaseolus vulgaris L.) proteins. *Food Hydrocolloids*, *119*, 106835. https://doi.org/10.1016/J.FOODHYD.2021.106835

Güzel, M., & Akpınar, Ö. (2019). Valorisation of fruit by-products: Production characterization of pectins from fruit peels. *Food and Bioproducts Processing*, *115*, 126–133. https://doi.org/10.1016/J.FBP.2019.03.009

Hao, D., Ai, T., Goerner, F., Hu, X., Runge, V. M., & Tweedle, M. (2012). MRI contrast agents: Basic chemistry and safety. In *Journal of Magnetic Resonance Imaging* (Vol. 36, Issue 5, pp. 1060–1071). https://doi.org/10.1002/jmri.23725

He, H., Shi, J., Yu, S., Yang, J., Xu, K., He, C., & Li, X. (2024). Exploring green and efficient zero-dimensional carbon-based inhibitors for carbon steel: From performance to mechanism. *Construction and Building Materials*, *411*. https://doi.org/10.1016/j.conbuildmat.2023.134334

Henchion, M., Hayes, M., Mullen, A. M., Fenelon, M., & Tiwari, B. (2017). Future protein supply and demand: Strategies and factors influencing a sustainable equilibrium. *Foods*, *6*(7), 1–21. https://doi.org/10.3390/foods6070053

Indrawati, L., Stroshine, R. L., & Narsimhan, G. (2007). Low-field NMR: A tool for studying protein aggregation. *Journal of the Science of Food and Agriculture*, *87*(12), 2207–2216. https://doi.org/10.1002/jsfa.2914

Jeske, S., Zannini, E., & Arendt, E. K. (2017). Evaluation of Physicochemical and Glycaemic Properties of Commercial Plant-Based Milk Substitutes. *Plant Foods for Human Nutrition*, *72*(1), 26–33. https://doi.org/10.1007/s11130-016-0583-0

Jiang, J., Xiong, Y. L., & Chen, J. (2010). pH Shifting alters solubility characteristics and thermal stability of soy protein isolate and its globulin fractions in different pH, salt concentration, and temperature conditions. *Journal of Agricultural and Food Chemistry*, *58*(13), 8035–8042. https://doi.org/10.1021/JF101045B

Jung, B. A., & Weigel, M. (2013). Spin echo magnetic resonance imaging. In *Journal of Magnetic Resonance Imaging* (Vol. 37, Issue 4, pp. 805–817). https://doi.org/10.1002/jmri.24068

Kirtil, E., & Oztop, M. H. (2016). 1H Nuclear Magnetic Resonance Relaxometry and Magnetic Resonance Imaging and Applications in Food Science and Processing. In *Food Engineering Reviews* (Vol. 8, Issue 1, pp. 1–22). Springer New York LLC. https://doi.org/10.1007/s12393-015-9118-y

Krebs, M. R. H., Devlin, G. L., & Donald, A. M. (2007). Protein particulates: Another generic form of protein aggregation? *Biophysical Journal*, *92*(4), 1336–1342. https://doi.org/10.1529/biophysj.106.094342

Kuo, Y. T., Herlihy, A. H., So, P. W., Bhakoo, K. K., & Bell, J. D. (2005). In vivo measurements of T1 relaxation times in mouse brain associated with different modes of systemic administration of manganese chloride. *Journal of Magnetic Resonance Imaging*, *21*(4), 334–339. https://doi.org/10.1002/jmri.20285

Lan, Y., Chen, B., & Rao, J. (2018a). Pea protein isolate–high methoxyl pectin soluble complexes for improving pea protein functionality: Effect of pH, biopolymer ratio and concentrations. *Food Hydrocolloids*, *80*, 245–253. https://doi.org/10.1016/j.foodhyd.2018.02.021

Lan, Y., Chen, B., & Rao, J. (2018b). Pea protein isolate–high methoxyl pectin soluble complexes for improving pea protein functionality: Effect of pH, biopolymer ratio and concentrations. *Food Hydrocolloids*, *80*, 245–253. https://doi.org/10.1016/j.foodhyd.2018.02.021

Larson, N. R., Wei, Y., & Middaugh, C. R. (2018). Label-Free, Direct Measurement of Protein Concentrations in Turbid Solutions with a UV-Visible Integrating Cavity Absorbance Spectrometer. *Analytical Chemistry*, *90*(8), 4982–4986. https://doi.org/10.1021/ACS.ANALCHEM.8B00502/SUPPL_FILE/AC8B00502_SI_001.PDF

Laukien, D. D., & Tschopp, W. H. (1993). *Concepts in Magnetic Resonance* (Vol. 6).

Ma, K. K., Greis, M., Lu, J., Nolden, A. A., McClements, D. J., & Kinchla, A. J. (2022). Functional Performance of Plant Proteins. In *Foods* (Vol. 11, Issue 4). MDPI. https://doi.org/10.3390/foods11040594

Mäkinen, O. E., Wanhalinna, V., Zannini, E., & Arendt, E. K. (2016). Foods for Special Dietary Needs: Non-dairy Plant-based Milk Substitutes and Fermented Dairy-type Products. *Critical Reviews in Food Science and Nutrition*, *56*(3), 339–349. https://doi.org/10.1080/10408398.2012.761950

March, D., Bianco, V., & Franzese, G. (2021). Protein Unfolding and Aggregation near a Hydrophobic Interface. *Polymers*, *13*(1), 1–14. https://doi.org/10.3390/POLYM13010156

McClements, D. J. (2018). Encapsulation, protection, and delivery of bioactive proteins and peptides using nanoparticle and microparticle systems: A review. In *Advances in Colloid and Interface Science* (Vol. 253, pp. 1–22). Elsevier B.V. https://doi.org/10.1016/j.cis.2018.02.002

McClements, D. J., & Keogh, M. K. (1995). Physical properties of cold-setting gels formed from heat-denatured whey protein isolate. *Journal of the Science of Food and Agriculture*, *69*(1), 7–14. https://doi.org/10.1002/JSFA.2740690103

Mession, J. L., Assifaoui, A., Lafarge, C., Saurel, R., & Cayot, P. (2012). Protein aggregation induced by phase separation in a pea proteins-sodium alginate-water ternary system. *Food Hydrocolloids*, *28*(2), 333–343. https://doi.org/10.1016/j.foodhyd.2011.12.022

Munialo, C. D., Martin, A. H., Van Der Linden, E., & De Jongh, H. H. J. (2014). Fibril formation from pea protein and subsequent gel formation. *Journal of Agricultural and Food Chemistry*, *62*(11), 2418–2427. https://doi.org/10.1021/JF4055215/ASSET/IMAGES/MEDIUM/JF-2013-055215_0009.GIF

Ozel, B., & Oztop, M. H. (2021). A quick look to the use of time domain nuclear magnetic resonance relaxometry and magnetic resonance imaging for food quality applications. In *Current Opinion in Food Science* (Vol. 41, pp. 122–129). Elsevier Ltd. https://doi.org/10.1016/j.cofs.2021.03.012

Patel, K. K., Khan, M. A., & Kar, A. (2015). Recent developments in applications of MRI techniques for foods and agricultural produce—an overview. In *Journal of Food Science and Technology* (Vol. 52, Issue 1, pp. 1–26). Springer. https://doi.org/10.1007/s13197-012-0917-3

Patrignani, F., & Lanciotti, R. (2016). Applications of high and ultra high pressure homogenization for food safety. In *Frontiers in Microbiology* (Vol. 7). Frontiers Media S.A. https://doi.org/10.3389/fmicb.2016.01132

Pautler, R. G., Silva, A. C., & Koretsky, A. P. (1998). In vivo neuronal tract tracing using manganese-enhanced magnetic resonance imaging. *Magnetic Resonance in Medicine*, *40*(5), 740–748. https://doi.org/10.1002/MRM.1910400515

Plewes, D. B. (1994). The AAPM/RSNA physics tutorial for residents. Contrast mechanisms in spin-echo MR imaging.

*Https://Doi.Org/10.1148/Radiographics.14.6.7855348*, *14*(6). https://doi.org/10.1148/RADIOGRAPHICS.14.6.7855348

Qiu, W., Zhang, L., Kao, Y. T., Lu, W., Li, T., Kim, J., Sollenberger, G. M., Wang, L., & Zhong, D. (2005). Ultrafast hydration dynamics in melittin folding and aggregation: helix formation and tetramer self-assembly. *The Journal of Physical Chemistry. B*, *109*(35), 16901–16910. https://doi.org/10.1021/JP0511754

Ridgway, J. P. (2015). Generating a Signal: RF Pulses and Echoes. *Cardiovascular MR Manual*, 21–29. https://doi.org/10.1007/978-3-319-20940-1_4

Saio, T., Guan, X., Rossi, P., Economou, A., & Kalodimos, C. G. (2014). Structural basis for protein antiaggregation activity of the trigger factor chaperone. *Science*, *344*(6184). https://doi.org/10.1126/SCIENCE.1250494/SUPPL_FILE/SAIO.SM.PDF

Seeger, L. L. (1989). Physical principles of magnetic resonance imaging. *Clinical Orthopaedics and Related Research®*, *244*(NA;), 7–16. https://doi.org/10.1097/00003086-198907000-00003

Soltner, H., & Blümler, P. (2010). Dipolar Halbach magnet stacks made from identically shaped permanent magnets for magnetic resonance. *Concepts in Magnetic Resonance Part A: Bridging Education and Research*, *36*(4), 211–222. https://doi.org/10.1002/cmr.a.20165

Sun, H., AlZubaidi, A., Purchase, A., & Sharp, J. C. (2020). A geometrically decoupled, twisted solenoid single-axis gradient coil set for TRASE. *Magnetic Resonance in Medicine*, *83*(4), 1484–1498. https://doi.org/10.1002/mrm.28003

Szuminska, K., Gutszeb, A., & Kowalczyk3, A. (2001). Relaxation of Water Protons in Highly Concentrated Aqueous Protein Systems Studied by NMR Spectroscopy. In *Z. Naturforsch* (Vol. 56). www.znaturforsch.com

Utrera, M., & Estévez, M. (2012). Oxidation of myofibrillar proteins and impaired functionality: Underlying mechanisms of the carbonylation pathway. *Journal of Agricultural and Food Chemistry*, *60*(32), 8002–8011. https://doi.org/10.1021/JF302111J/ASSET/IMAGES/LARGE/JF-2012-02111J_0004.JPEG

Wilkinson-Smith, V. C., Major, G., Ashleigh, L., Murray, K., Hoad, C. L., Marciani, L., Gowland, P. A., & Spiller, R. C. (2018). Insights Into the Different Effects of Food on Intestinal Secretion Using Magnetic Resonance Imaging. *Journal of Parenteral and Enteral Nutrition*, *42*(8), 1342–1348. https://doi.org/10.1002/jpen.1157

Wu, G., Bazer, F. W., & Cross, H. R. (2014). Land-based production of animal protein: Impacts, efficiency, and sustainability. *Annals of the New York Academy of Sciences*, *1328*(1), 18–28. https://doi.org/10.1111/nyas.12566

Wu, K. P., & Baum, J. (2010). Detection of transient interchain interactions in the intrinsically disordered protein α-synuclein by NMR paramagnetic relaxation enhancement. *Journal of the American Chemical Society*, *132*(16), 5546–5547. https://doi.org/10.1021/ja9105495

Xiao, Y. D., Paudel, R., Liu, J., Ma, C., Zhang, Z. S., & Zhou, S. K. (2016). MRI contrast agents: Classification and application (Review). In *International Journal of Molecular Medicine* (Vol. 38, Issue 5, pp. 1319–1326). Spandidos Publications. https://doi.org/10.3892/ijmm.2016.2744

Yan, G. P., Robinson, L., & Hogg, P. (2007). Magnetic resonance imaging contrast agents: Overview and perspectives. In *Radiography* (Vol. 13, Issue SUPPLL. 1). https://doi.org/10.1016/j.radi.2006.07.005

Zhang, Z., Yang, Y., Huang, X., Jin, Z., & Jiao, A. (2023). Stabilization of a collagen peptide-cranberry juice by three functional polysaccharides with different charge characteristics. *Food Hydrocolloids*, *139*. https://doi.org/10.1016/j.foodhyd.2023.108518

# APPENDICES

## A. Optimized dimensional schematic of actual Halbach Array which is built

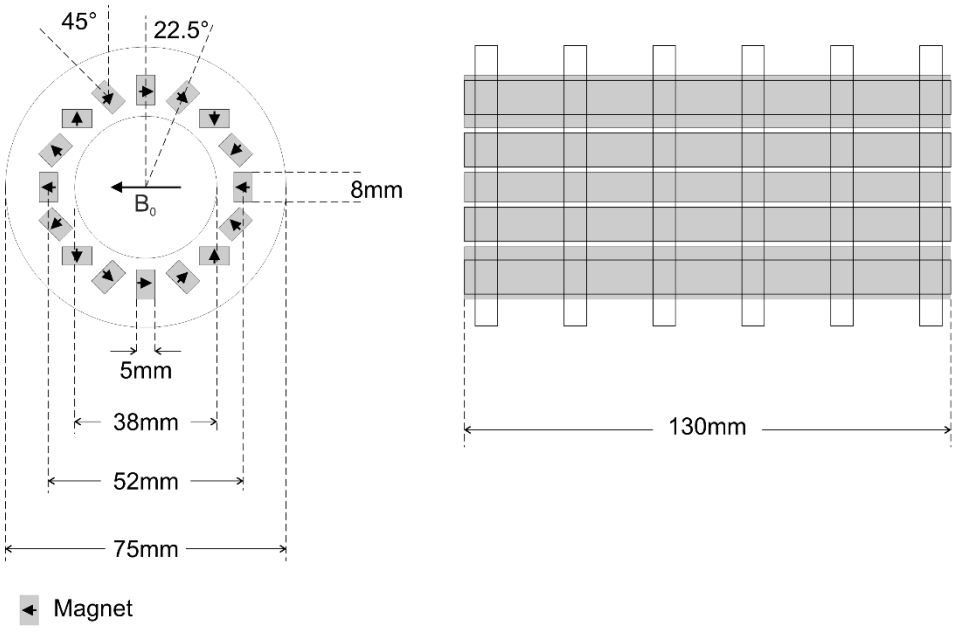


Figure A.1 Schematic of actual Halbach Array

## B. Statistical Analysis (ANOVA Results)

### Probability Plot of SRES

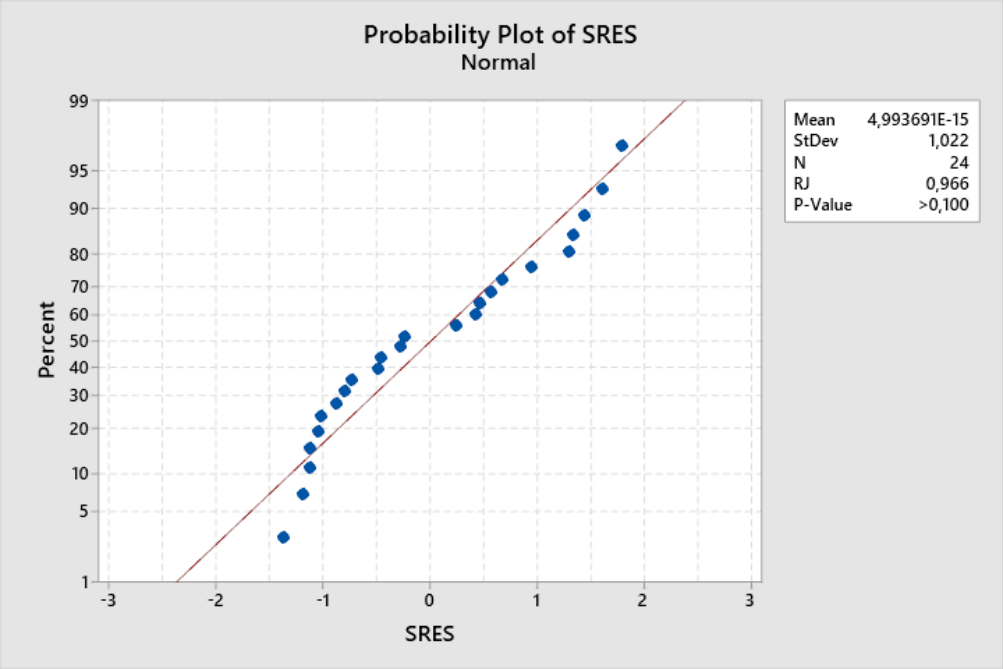


## General Linear Model: brix versus Time

### Method

Factor coding (-1; 0; +1)

### Factor Information

| Factor | Type | Levels | Values |
|---|---|---|---|
| Time | Fixed | 8 | 0,00; 2,50; 5,00; 7,50; 10,00; 12,50; 15,00; 17,50 |

### Analysis of Variance

| Source | DF | Adj SS | Adj MS | F-Value | P-Value |
|---|---|---|---|---|---|
| Time | 7 | 57,0666 | 8,15237 | 344,77 | 0,000 |
| Error | 16 | 0,3783 | 0,02365 | | |
| Total | 23 | 57,4449 | | | |

### Model Summary

| S | R-sq | R-sq(adj) | R-sq(pred) |
|---|---|---|---|
| 0,153772 | 99,34% | 99,05% | 98,52% |

### Coefficients

| Term | Coef | SE Coef | T-Value | P-Value | VIF |
|---|---|---|---|---|---|
| Constant | 68,2604 | 0,0314 | 2174,69 | 0,000 | |
| Time | | | | | |
| 0,00 | -2,6271 | 0,0830 | -31,63 | 0,000 | 1,75 |
| 2,50 | -1,8604 | 0,0830 | -22,40 | 0,000 | 1,75 |
| 5,00 | -0,7937 | 0,0830 | -9,56 | 0,000 | 1,75 |
| 7,50 | -0,1104 | 0,0830 | -1,33 | 0,202 | 1,75 |
| 10,00 | 0,7729 | 0,0830 | 9,31 | 0,000 | 1,75 |
| 12,50 | 1,2063 | 0,0830 | 14,53 | 0,000 | 1,75 |
| 15,00 | 1,4396 | 0,0830 | 17,33 | 0,000 | 1,75 |

### Regression Equation

brix = 68,2604 - 2,6271 Time_0,00 - 1,8604 Time_2,50 - 0,7937 Time_5,00 - 0,1104 Time_7,50
+ 0,7729 Time_10,00 + 1,2063 Time_12,50 + 1,4396 Time_15,00 + 1,9729 Time_17,50

### Fits and Diagnostics for Unusual Observations

| Obs | brix | Fit | Resid | Std Resid | |
|---|---|---|---|---|---|
| 10 | 66,8000 | 66,4000 | 0,4000 | 3,19 | R |

*R Large residual*

## Comparisons for brix

### Tukey Pairwise Comparisons: Time

### Grouping Information Using the Tukey Method and 95% Confidence

| Time | N | Mean | Grouping | | | | | |
|---|---|---|---|---|---|---|---|---|
| 17,50 | 3 | 70,2333 | A | | | | | |
| 15,00 | 3 | 69,7000 | | B | | | | |
| 12,50 | 3 | 69,4667 | | B | C | | | |
| 10,00 | 3 | 69,0333 | | | C | | | |
| 7,50 | 3 | 68,1500 | | | | D | | |
| 5,00 | 3 | 67,4667 | | | | | E | |
| 2,50 | 3 | 66,4000 | | | | | | F |
| 0,00 | 3 | 65,6333 | | | | | | G |

*Means that do not share a letter are significantly different.*

## Probability Plot of SRES

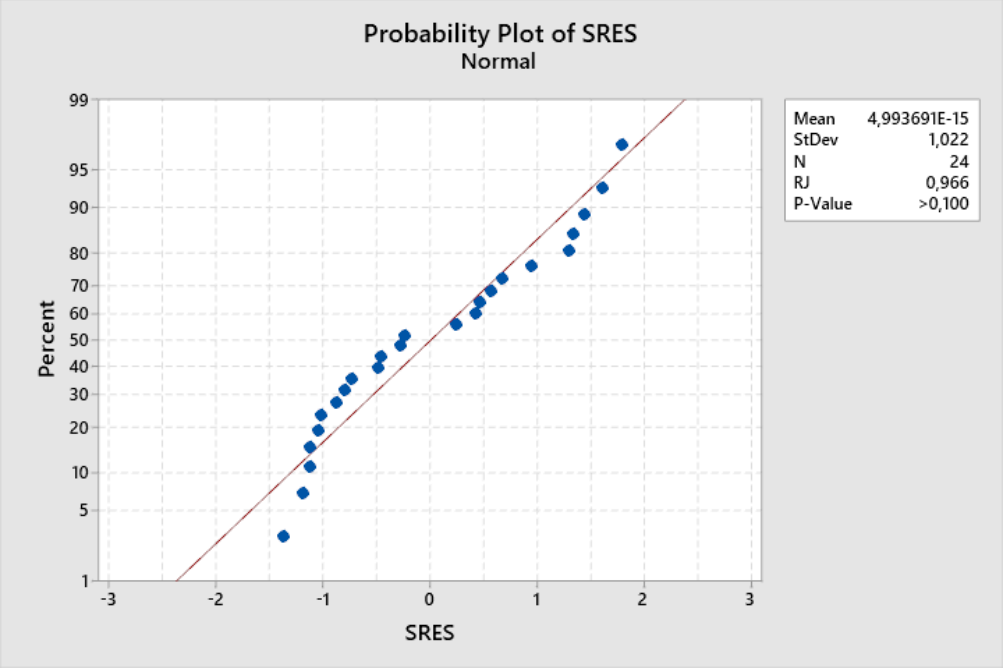


**GENERAL LİNEAR MODEL: $T_2$EFF (MS) VERSUS TİME**

**METHOD**

FACTOR (-1; 0; +1)

CODİNG

**FACTOR INFORMATİON**

| FACTOR | TYPE | LEVELS | VALUES |
|---|---|---|---|

| | | | |
|---|---|---|---|
| TİME | FİXED | 8 | 0,00; 2,50; 5,00; 7,50; 10,00; 12,50; 15,00; 17,50 |

**ANALYSİS OF VARİANCE**

| SOURCE | DF | ADJ SS | ADJ MS | F-VALUE | P-VALUE |
|---|---|---|---|---|---|
| TİME | 7 | 318,12 | 45,445 | 33,63 | 0,000 |
| ERROR | 16 | 21,62 | 1,351 | | |
| TOTAL | 23 | 339,74 | | | |

**MODEL SUMMARY**

| S | R-SQ | R-SQ(ADJ) | R-SQ(PRED) |
|---|---|---|---|
| 1,16243 | 93,64% | 90,85% | 85,68% |

**COEFFİCİENTS**

| TERM | COEF | SE COEF | T-VALUE | P-VALUE | VIF |
|---|---|---|---|---|---|
| CONSTANT | 31,242 | 0,237 | 131,67 | 0,000 | |
| TİME | | | | | |
| 0,00 | 6,525 | 0,628 | 10,39 | 0,000 | 1,75 |
| 2,50 | 3,325 | 0,628 | 5,30 | 0,000 | 1,75 |
| 5,00 | 1,958 | 0,628 | 3,12 | 0,007 | 1,75 |
| 7,50 | 0,758 | 0,628 | 1,21 | 0,245 | 1,75 |
| 10,00 | -1,075 | 0,628 | -1,71 | 0,106 | 1,75 |
| 12,50 | -2,508 | 0,628 | -4,00 | 0,001 | 1,75 |
| 15,00 | -4,175 | 0,628 | -6,65 | 0,000 | 1,75 |

**REGRESSİON EQUATİON**

$T_2$EFF (MS) = 31,242 + 6,525 TİME_0,00 + 3,325 TİME_2,50 + 1,958 TİME_5,00 + 0,758 TİME_7,50
- 1,075 TİME_10,00 - 2,508 TİME_12,50 - 4,175 TİME_15,00 - 4,808 TİME_17,50

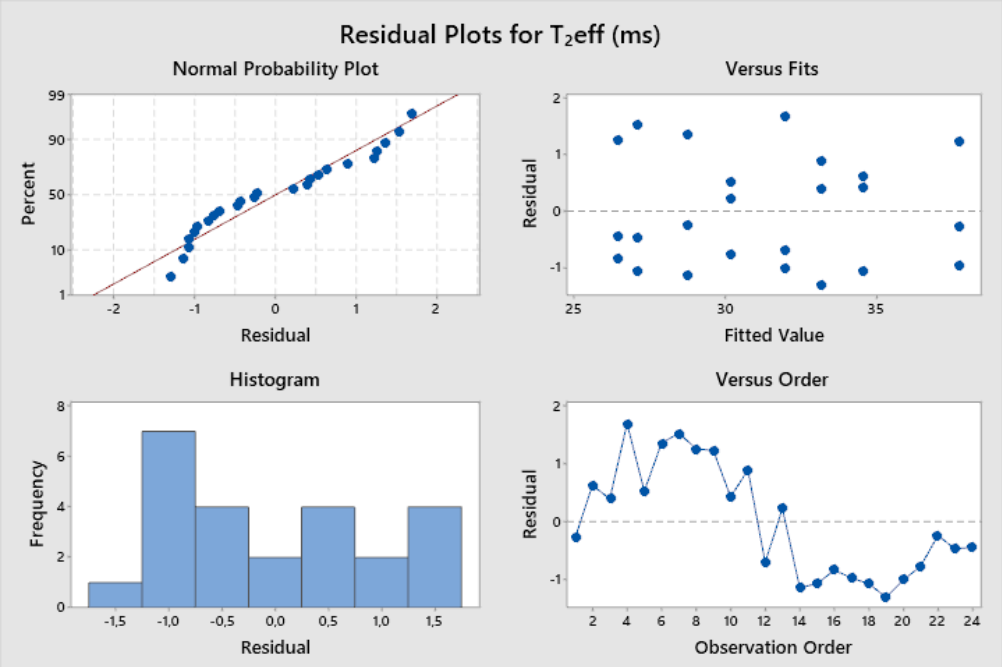


**GENERAL LINEAR MODEL: ABSORBANCE(%4) VERSUS TIME**

**METHOD**

| | |
|---|---|
| FACTOR CODING | (-1; 0; +1) |

**FACTOR INFORMATION**

| FACTOR | TYPE | LEVELS | VALUES |
|---|---|---|---|
| TIME | FIXED | 4 | 1; 4; 7; 24 |

**ANALYSIS OF VARIANCE**

| SOURCE | DF | ADJ SS | ADJ MS | F-VALUE | P-VALUE |
|---|---|---|---|---|---|
| TIME | 3 | 0,079216 | 0,026405 | 90,31 | 0,000 |
| ERROR | 8 | 0,002339 | 0,000292 | | |
| TOTAL | 11 | 0,081555 | | | |

**MODEL SUMMARY**

| S | R-SQ | R-SQ(ADJ) | R-SQ(PRED) |
|---|---|---|---|
| 0,0170992 | 97,13% | 96,06% | 93,55% |

**COEFFICIENTS**

| TERM | COEF | SE COEF | T-VALUE | P-VALUE | VIF |
|---|---|---|---|---|---|
| CONSTANT | 1,64372 | 0,00494 | 333,00 | 0,000 | |
| TIME | | | | | |
| 1 | 0,11742 | 0,00855 | 13,73 | 0,000 | 1,50 |
| 4 | -0,05812 | 0,00855 | -6,80 | 0,000 | 1,50 |
| 7 | 0,03152 | 0,00855 | 3,69 | 0,006 | 1,50 |

**REGRESSION EQUATION**

ABSORBANCE(%4) = 1,64372 + 0,11742 TIME_1 - 0,05812 TIME_4 + 0,03152 TIME_7 - 0,09082 TIME_24

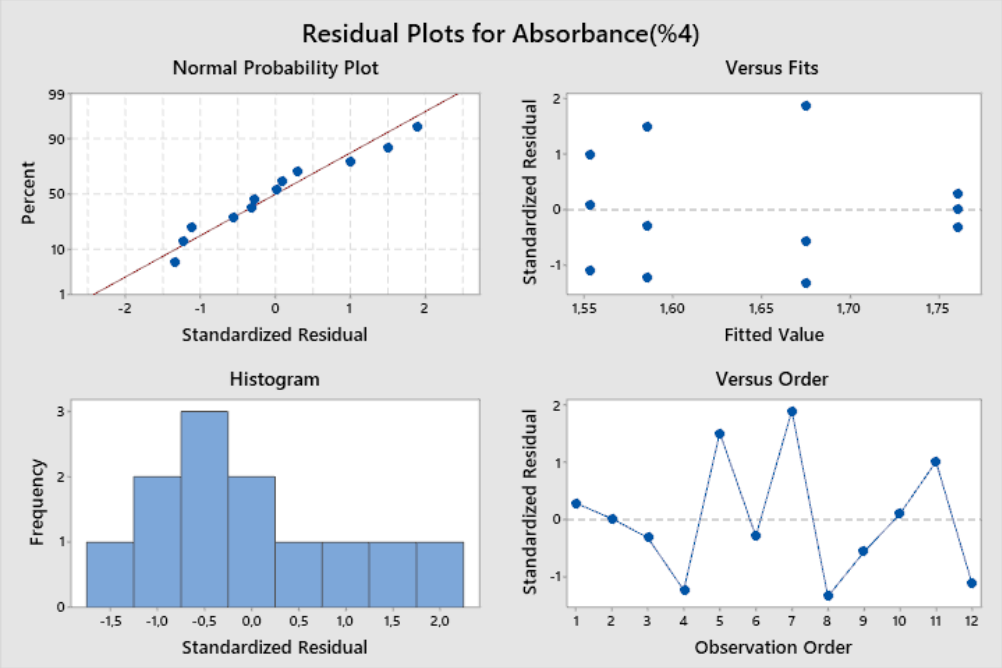


WORKSHEET 1

**COMPARİSONS FOR $T_2$EFF (MS)**

**TUKEY PAİRWİSE COMPARİSONS: TİME**

**GROUPİNG INFORMATİON USİNG THE TUKEY METHOD AND 95% CONFİDENCE**

| TİME | N | MEAN | GROUPİNG | | | | |
|---|---|---|---|---|---|---|---|
| 0,00 | 3 | 37,7667 | A | | | | |
| 2,50 | 3 | 34,5667 | A | B | | | |
| 5,00 | 3 | 33,2000 | | B | C | | |
| 7,50 | 3 | 32,0000 | | B | C | D | |
| 10,00 | 3 | 30,1667 | | | C | D | E |
| 12,50 | 3 | 28,7333 | | | | D | E F |
| 15,00 | 3 | 27,0667 | | | | | E F |
| 17,50 | 3 | 26,4333 | | | | | F |

*MEANS THAT DO NOT SHARE A LETTER ARE SİGNİFİCANTLY DİFFERENT.*

## Regression Analysis: $T_2$eff (ms) versus Brix

The regression equation is

$T_2$eff (ms) = 194,1 - 2,387 Brix

### Model Summary

| S | R-sq | R-sq(adj) |
|---|---|---|
| 1,17961 | 91,13% | 90,73% |

### Analysis of Variance

| Source | DF | SS | MS | F | P |
|---|---|---|---|---|---|

| | | | | | |
|---|---|---|---|---|---|
| Regression | 1 | 314,601 | 314,601 | 226,09 | 0,000 |
| Error | 22 | 30,612 | 1,391 | | |
| Total | 23 | 345,213 | | | |

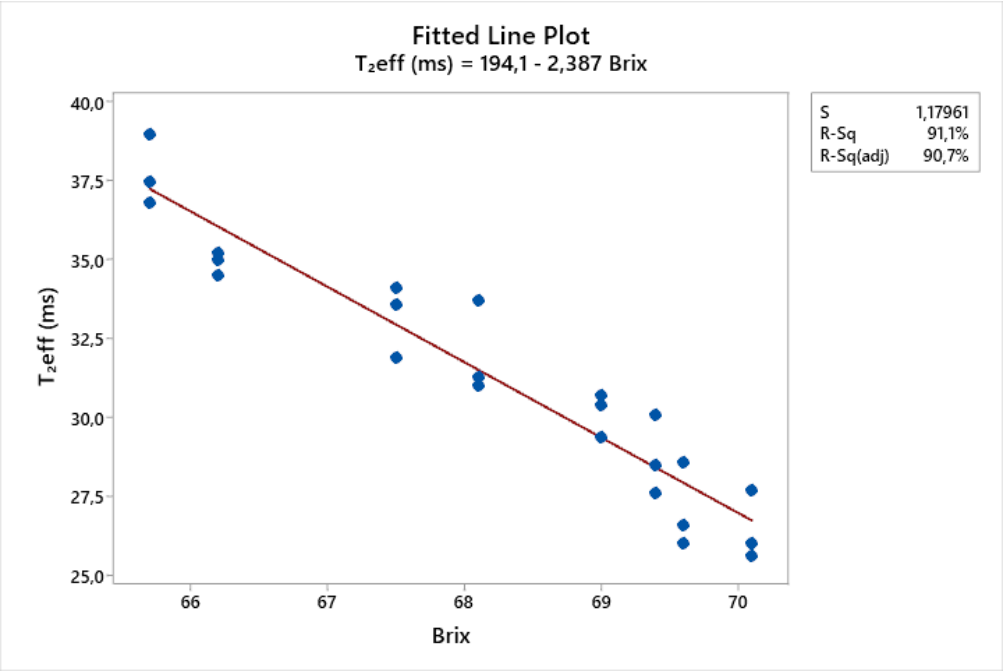


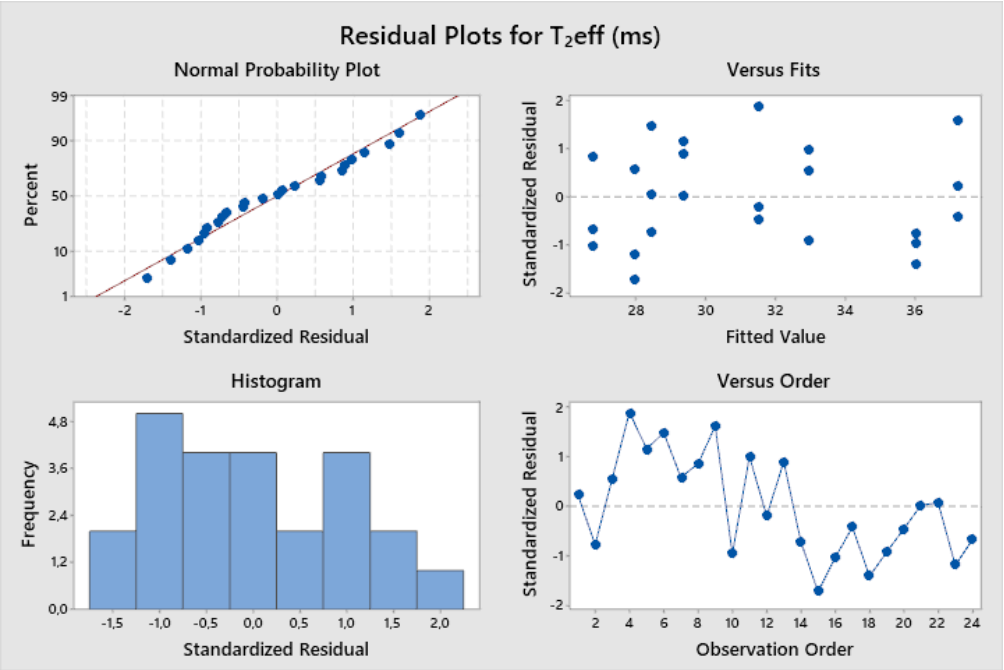


WORKSHEET 6

## Comparisons for Absorbance(%4)

### Tukey Pairwise Comparisons: Time

### Grouping Information Using the Tukey Method and 95% Confidence

| Time | N | Mean | Grouping | | |
|---|---|---|---|---|---|
| 1 | 3 | 1,76113 | A | | |
| 7 | 3 | 1,67523 | | B | |
| 4 | 3 | 1,58560 | | | C |
| 24 | 3 | 1,55290 | | | C |

*Means that do not share a letter are significantly different.*

## General Linear Model: Mean_Intensity versus Time; Conc

### Method

Factor coding (-1; 0; +1)

### Factor Information

| Factor | Type | Levels | Values |
|---|---|---|---|
| Time | Fixed | 4 | 1; 4; 7; 24 |
| Conc | Fixed | 3 | 0; 2; 4 |

### Analysis of Variance

| Source | DF | Adj SS | Adj MS | F-Value | P-Value |
|---|---|---|---|---|---|
| Time | 3 | 0,000000 | 0,000000 | 47,69 | 0,000 |
| Conc | 2 | 0,000000 | 0,000000 | 1441,64 | 0,000 |
| Time*Conc | 6 | 0,000000 | 0,000000 | 15,17 | 0,000 |
| Error | 24 | 0,000000 | 0,000000 | | |
| Total | 35 | 0,000000 | | | |

### Model Summary

| S | R-sq | R-sq(adj) | R-sq(pred) |
|---|---|---|---|
| 0,0000000 | 99,24% | 98,89% | 98,28% |

### Coefficients

| Term | Coef | SE Coef | T-Value | P-Value | VIF |
|---|---|---|---|---|---|
| Constant | 0,000001 | 0,000000 | 547,47 | 0,000 | |
| Time | | | | | |
| 1 | 0,000000 | 0,000000 | 3,19 | 0,004 | 1,50 |
| 4 | 0,000000 | 0,000000 | 6,51 | 0,000 | 1,50 |
| 7 | 0,000000 | 0,000000 | 1,89 | 0,070 | 1,50 |
| Conc | | | | | |
| 0 | 0,000000 | 0,000000 | 48,59 | 0,000 | 1,33 |
| 2 | -0,000000 | 0,000000 | -4,50 | 0,000 | 1,33 |
| Time*Conc | | | | | |
| 1 0 | -0,000000 | 0,000000 | -2,81 | 0,010 | 2,00 |
| 1 2 | 0,000000 | 0,000000 | 6,12 | 0,000 | 2,00 |
| 4 0 | -0,000000 | 0,000000 | -4,54 | 0,000 | 2,00 |
| 4 2 | 0,000000 | 0,000000 | 0,32 | 0,752 | 2,00 |
| 7 0 | 0,000000 | 0,000000 | 0,15 | 0,882 | 2,00 |
| 7 2 | -0,000000 | 0,000000 | -2,13 | 0,044 | 2,00 |

### Regression Equation

Mean_Intensity = 0,000001 + 0,000000 Time_1 + 0,000000 Time_4 + 0,000000 Time_7
- 0,000000 Time_24 + 0,000000 Conc_0 - 0,000000 Conc_2 - 0,000000 Conc_4
- 0,000000 Time*Conc_1 0 + 0,000000 Time*Conc_1 2 - 0,000000 Time*Conc_1 4
- 0,000000 Time*Conc_4 0 + 0,000000 Time*Conc_4 2 + 0,000000 Time*Conc_4 4
+ 0,000000 Time*Conc_7 0 - 0,000000 Time*Conc_7 2 + 0,000000 Time*Conc_7 4
+ 0,000000 Time*Conc_24 0 - 0,000000 Time*Conc_24 2 - 0,000000 Time*Conc_24 4

### Fits and Diagnostics for Unusual Observations

| Obs | Mean_Intensity | Fit | Resid | Std Resid | |
|---|---|---|---|---|---|
| 2 | 0,000002 | 0,000002 | 0,000000 | 2,25 | R |
| 15 | 0,000001 | 0,000001 | -0,000000 | -2,23 | R |

*R Large residual*

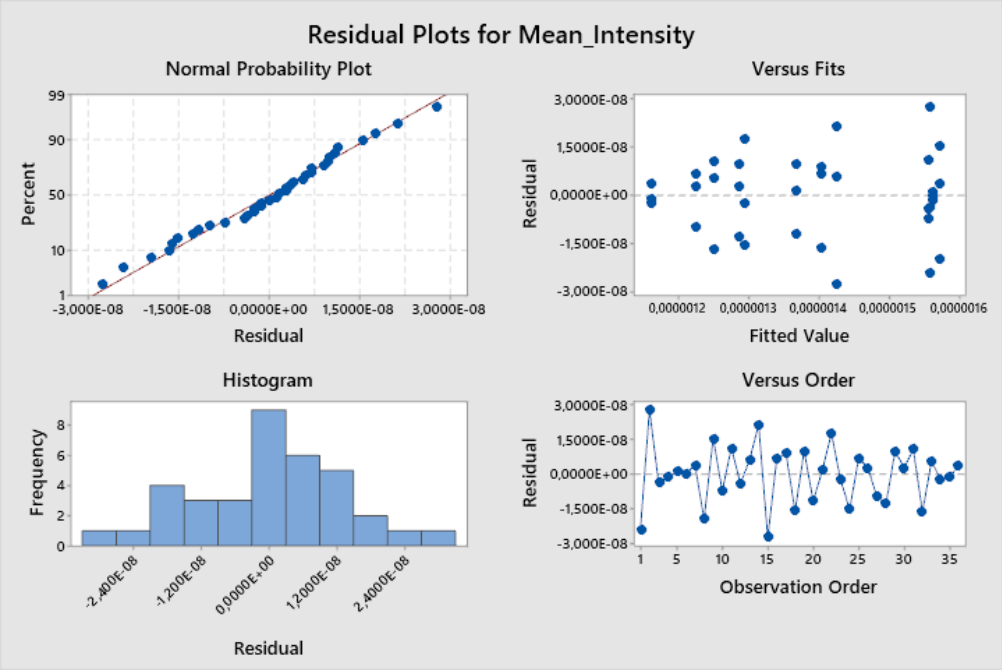


## Comparisons for Mean_Intensity

### Tukey Pairwise Comparisons: Time

### Grouping Information Using the Tukey Method and 95% Confidence

| Time | N | Mean | Grouping | | |
|---|---|---|---|---|---|
| 4 | 9 | 0,0000014 | A | | |
| 1 | 9 | 0,0000014 | A | B | |
| 7 | 9 | 0,0000014 | | B | |
| 24 | 9 | 0,0000013 | | | C |

*Means that do not share a letter are significantly different.*

### Tukey Pairwise Comparisons: Conc

### Grouping Information Using the Tukey Method and 95% Confidence

| Conc | N | Mean | Grouping | | |
|---|---|---|---|---|---|
| 0 | 12 | 0,0000016 | A | | |
| 2 | 12 | 0,0000014 | | B | |
| 4 | 12 | 0,0000012 | | | C |

*Means that do not share a letter are significantly different.*

### Tukey Pairwise Comparisons: Time*Conc

### Grouping Information Using the Tukey Method and 95% Confidence

| Time*Conc | N | Mean | Grouping |
|---|---|---|---|

| | | | | | | |
|---|---|---|---|---|---|---|
| 7 0 | 3 | 0,0000016 | A | | | |
| 4 0 | 3 | 0,0000016 | A | | | |
| 1 0 | 3 | 0,0000016 | A | | | |
| 24 0 | 3 | 0,0000016 | A | | | |
| 1 2 | 3 | 0,0000014 | | B | | |
| 4 2 | 3 | 0,0000014 | | B | C | |
| 7 2 | 3 | 0,0000014 | | | C | |
| 24 2 | 3 | 0,0000013 | | | | D |
| 4 4 | 3 | 0,0000013 | | | | D |
| 7 4 | 3 | 0,0000013 | | | | D | E |
| 1 4 | 3 | 0,0000012 | | | | | E |
| 24 4 | 3 | 0,0000012 | | | | | | F |

*Means that do not share a letter are significantly different.*

# General Linear Model: Mean_Intensity versus Time; Conc

## Method

Factor coding (-1; 0; +1)

## Factor Information

| Factor | Type | Levels | Values |
|---|---|---|---|
| Time | Fixed | 4 | 1; 4; 7; 24 |
| Conc | Fixed | 3 | 0; 2; 4 |

## Analysis of Variance

| Source | DF | Adj SS | Adj MS | F-Value | P-Value |
|---|---|---|---|---|---|
| Time | 3 | 0,000000 | 0,000000 | 223,88 | 0,000 |
| Conc | 2 | 0,000000 | 0,000000 | 1437,95 | 0,000 |
| Time*Conc | 6 | 0,000000 | 0,000000 | 173,94 | 0,000 |
| Error | 24 | 0,000000 | 0,000000 | | |
| Total | 35 | 0,000000 | | | |

## Model Summary

| S | R-sq | R-sq(adj) | R-sq(pred) |
|---|---|---|---|
| 0,0000000 | 99,48% | 99,24% | 98,83% |

## Coefficients

| Term | Coef | SE Coef | T-Value | P-Value | VIF |
|---|---|---|---|---|---|
| Constant | 0,000001 | 0,000000 | 383,27 | 0,000 | |
| Time | | | | | |
| 1 | -0,000000 | 0,000000 | -23,65 | 0,000 | 1,50 |
| 4 | 0,000000 | 0,000000 | 3,25 | 0,003 | 1,50 |
| 7 | 0,000000 | 0,000000 | 2,53 | 0,018 | 1,50 |
| Conc | | | | | |
| 0 | -0,000000 | 0,000000 | -37,51 | 0,000 | 1,33 |
| 2 | -0,000000 | 0,000000 | -14,44 | 0,000 | 1,33 |
| Time*Conc | | | | | |
| 1 0 | 0,000000 | 0,000000 | 18,63 | 0,000 | 2,00 |
| 1 2 | 0,000000 | 0,000000 | 12,17 | 0,000 | 2,00 |
| 4 0 | -0,000000 | 0,000000 | -2,08 | 0,048 | 2,00 |
| 4 2 | -0,000000 | 0,000000 | -6,26 | 0,000 | 2,00 |
| 7 0 | -0,000000 | 0,000000 | -2,48 | 0,020 | 2,00 |
| 7 2 | -0,000000 | 0,000000 | -3,43 | 0,002 | 2,00 |

## Regression Equation

Mean_Intensity = 0,000001 - 0,000000 Time_1 + 0,000000 Time_4 + 0,000000 Time_7
+ 0,000000 Time_24 - 0,000000 Conc_0 - 0,000000 Conc_2 + 0,000000 Conc_4
+ 0,000000 Time*Conc_1 0 + 0,000000 Time*Conc_1 2 - 0,000000 Time*Conc_1 4
- 0,000000 Time*Conc_4 0 - 0,000000 Time*Conc_4 2 + 0,000000 Time*Conc_4 4

- 0,000000 Time*Conc_7 0 - 0,000000 Time*Conc_7 2 + 0,000000 Time*Conc_7 4
- 0,000000 Time*Conc_24 0 - 0,000000 Time*Conc_24 2 + 0,000000 Time*Conc_24 4

### Fits and Diagnostics for Unusual Observations

| Obs | Mean_Intensity | Fit | Resid | Std Resid | |
|---|---|---|---|---|---|
| 8 | 0,000001 | 0,000001 | -0,000000 | -2,09 | R |
| 23 | 0,000001 | 0,000001 | 0,000000 | 2,32 | R |

*R Large residual*

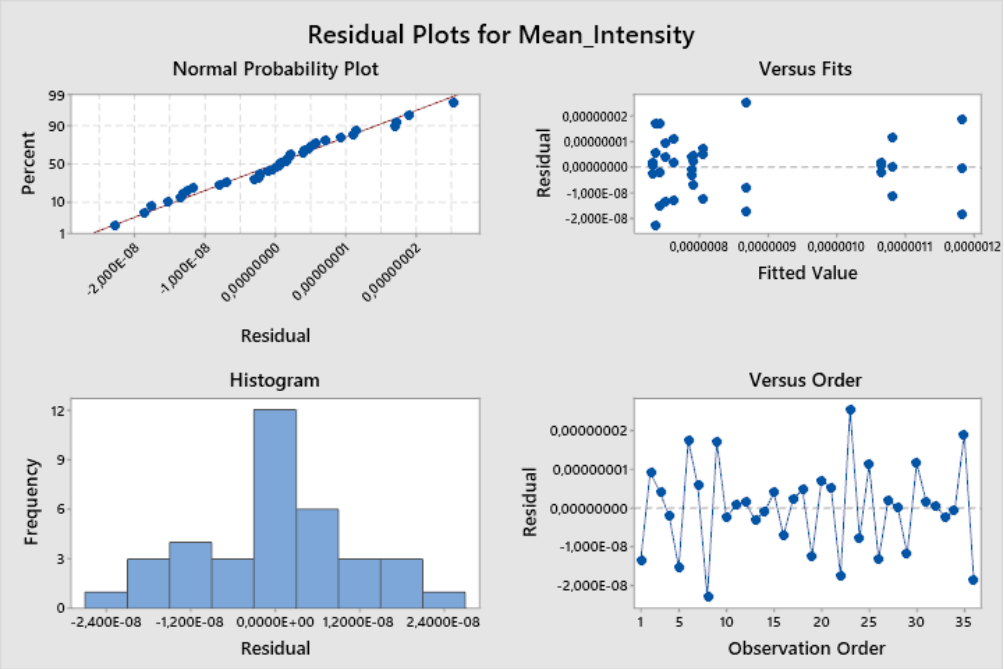


## Comparisons for Mean_Intensity

### Tukey Pairwise Comparisons: Time

### Grouping Information Using the Tukey Method and 95% Confidence

| Time | N | Mean | Grouping | | |
|---|---|---|---|---|---|
| 24 | 9 | 0,0000009 | A | | |
| 4 | 9 | 0,0000009 | | B | |
| 7 | 9 | 0,0000009 | | B | |
| 1 | 9 | 0,0000008 | | | C |

*Means that do not share a letter are significantly different.*

### Tukey Pairwise Comparisons: Conc

### Grouping Information Using the Tukey Method and 95% Confidence

| Conc | N | Mean | Grouping |
|---|---|---|---|
| 4 | 12 | 0,0000010 | A |

| | | | | |
|---|---|---|---|---|
| 2 | 12 | 0,0000008 | B | |
| 0 | 12 | 0,0000007 | | C |

*Means that do not share a letter are significantly different.*

### Tukey Pairwise Comparisons: Time*Conc

### Grouping Information Using the Tukey Method and 95% Confidence

| Time*Conc | N | Mean | Grouping | | | | |
|---|---|---|---|---|---|---|---|
| 24 4 | 3 | 0,0000012 | A | | | | |
| 4 4 | 3 | 0,0000011 | | B | | | |
| 7 4 | 3 | 0,0000011 | | B | | | |
| 24 2 | 3 | 0,0000009 | | | C | | |
| 7 2 | 3 | 0,0000008 | | | | D | |
| 4 2 | 3 | 0,0000008 | | | | D | E |
| 1 2 | 3 | 0,0000008 | | | | D | E F |
| 1 4 | 3 | 0,0000008 | | | | | E F G |
| 1 0 | 3 | 0,0000008 | | | | | F G |
| 4 0 | 3 | 0,0000007 | | | | | G |
| 7 0 | 3 | 0,0000007 | | | | | G |
| 24 0 | 3 | 0,0000007 | | | | | G |

*Means that do not share a letter are significantly different.*

## General Linear Model: D [3;2] versus Conc; Time

### Method

Factor coding (-1; 0; +1)

### Factor Information

| Factor | Type | Levels | Values |
|---|---|---|---|
| Conc | Fixed | 2 | 2; 4 |
| Time | Fixed | 4 | 1; 4; 7; 24 |

### Analysis of Variance

| Source | DF | Adj SS | Adj MS | F-Value | P-Value |
|---|---|---|---|---|---|
| Conc | 1 | 10,6400 | 10,6400 | 12790,40 | 0,000 |
| Time | 3 | 2,1440 | 0,7147 | 859,12 | 0,000 |
| Conc*Time | 3 | 1,5292 | 0,5097 | 612,76 | 0,000 |
| Error | 16 | 0,0133 | 0,0008 | | |
| Total | 23 | 14,3266 | | | |

### Model Summary

| S | R-sq | R-sq(adj) | R-sq(pred) |
|---|---|---|---|
| 0,0288422 | 99,91% | 99,87% | 99,79% |

### Coefficients

| Term | Coef | SE Coef | T-Value | P-Value | VIF |
|---|---|---|---|---|---|
| Constant | 1,42583 | 0,00589 | 242,18 | 0,000 | |
| Conc | | | | | |
| 2 | 0,66583 | 0,00589 | 113,09 | 0,000 | 1,00 |
| Time | | | | | |
| 1 | -0,3582 | 0,0102 | -35,12 | 0,000 | 1,50 |
| 4 | -0,2190 | 0,0102 | -21,48 | 0,000 | 1,50 |
| 7 | 0,2033 | 0,0102 | 19,94 | 0,000 | 1,50 |
| Conc*Time | | | | | |
| 2 1 | -0,3002 | 0,0102 | -29,44 | 0,000 | 1,50 |
| 2 4 | -0,1993 | 0,0102 | -19,55 | 0,000 | 1,50 |
| 2 7 | 0,2617 | 0,0102 | 25,66 | 0,000 | 1,50 |

### Regression Equation

D [3;2] = 1,42583 + 0,66583 Conc_2 - 0,66583 Conc_4 - 0,3582 Time_1 - 0,2190 Time_4
+ 0,2033 Time_7 + 0,3738 Time_24 - 0,3002 Conc*Time_2 1 - 0,1993 Conc*Time_2 4
+ 0,2617 Conc*Time_2 7 + 0,2378 Conc*Time_2 24 + 0,3002 Conc*Time_4 1
+ 0,1993 Conc*Time_4 4 - 0,2617 Conc*Time_4 7 - 0,2378 Conc*Time_4 24

### Fits and Diagnostics for Unusual Observations

| Obs | D [3;2] | Fit | Resid | Std Resid |
|---|---|---|---|---|
| 8 | 2,6300 | 2,5567 | 0,0733 | 3,11 R |
| 9 | 2,5000 | 2,5567 | -0,0567 | -2,41 R |

*R Large residual*

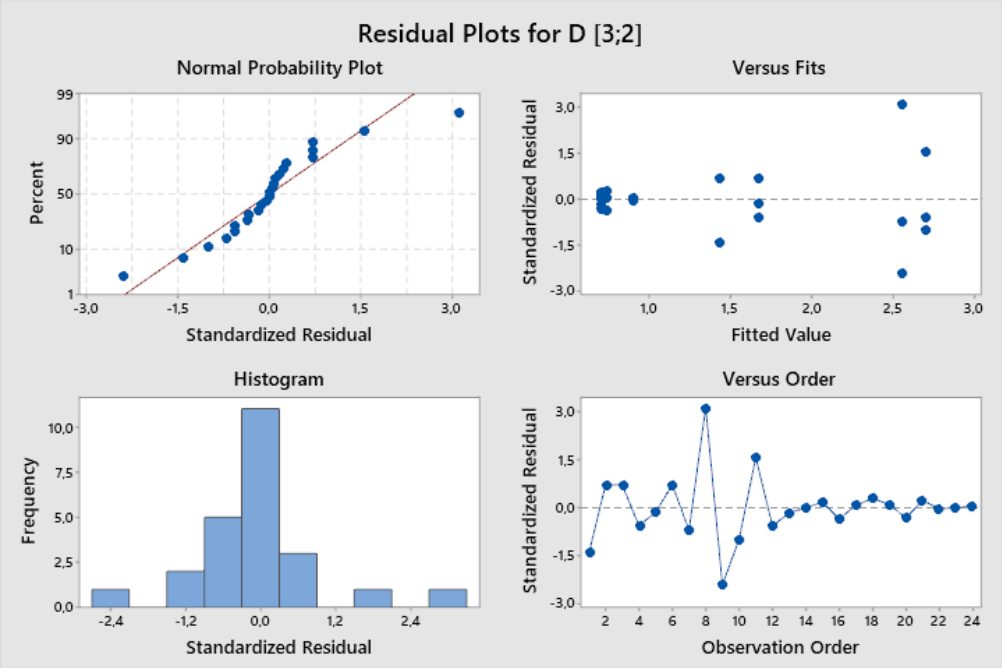


## Comparisons for D [3;2]

### Tukey Pairwise Comparisons: Conc

### Grouping Information Using the Tukey Method and 95% Confidence

| Conc | N | Mean | Grouping |
|---|---|---|---|
| 2 | 12 | 2,09167 | A |
| 4 | 12 | 0,76000 | B |

*Means that do not share a letter are significantly different.*

### Tukey Pairwise Comparisons: Time

### Grouping Information Using the Tukey Method and 95% Confidence

| Time | N | Mean | Grouping |
|---|---|---|---|
| 24 | 6 | 1,79967 | A |
| 7 | 6 | 1,62917 | B |

| | | | | |
|---|---|---|---|---|
| 4 | 6 | 1,20683 | C | |
| 1 | 6 | 1,06767 | | D |

*Means that do not share a letter are significantly different.*

### Tukey Pairwise Comparisons: Conc*Time

### Grouping Information Using the Tukey Method and 95% Confidence

| Conc*Time | N | Mean | Grouping | | | | |
|---|---|---|---|---|---|---|---|
| 2 24 | 3 | 2,70333 | A | | | | |
| 2 7 | 3 | 2,55667 | | B | | | |
| 2 4 | 3 | 1,67333 | | | C | | |
| 2 1 | 3 | 1,43333 | | | | D | |
| 4 24 | 3 | 0,89600 | | | | | E |
| 4 4 | 3 | 0,74033 | | | | | | F |
| 4 1 | 3 | 0,70200 | | | | | | F |
| 4 7 | 3 | 0,70167 | | | | | | F |

*Means that do not share a letter are significantly different.*

## General Linear Model: D [4;3] versus Conc; Time

### Method

Factor coding (-1; 0; +1)

### Factor Information

| Factor | Type | Levels | Values |
|---|---|---|---|
| Conc | Fixed | 2 | 2; 4 |
| Time | Fixed | 4 | 1; 4; 7; 24 |

### Analysis of Variance

| Source | DF | Adj SS | Adj MS | F-Value | P-Value |
|---|---|---|---|---|---|
| Conc | 1 | 49,9682 | 49,9682 | 4149,61 | 0,000 |
| Time | 3 | 35,5468 | 11,8489 | 983,99 | 0,000 |
| Conc*Time | 3 | 2,5041 | 0,8347 | 69,32 | 0,000 |
| Error | 16 | 0,1927 | 0,0120 | | |
| Total | 23 | 88,2118 | | | |

### Model Summary

| S | R-sq | R-sq(adj) | R-sq(pred) |
|---|---|---|---|
| 0,109735 | 99,78% | 99,69% | 99,51% |

### Coefficients

| Term | Coef | SE Coef | T-Value | P-Value | VIF |
|---|---|---|---|---|---|
| Constant | 6,2546 | 0,0224 | 279,23 | 0,000 | |
| Conc | | | | | |
| 2 | 1,4429 | 0,0224 | 64,42 | 0,000 | 1,00 |
| Time | | | | | |
| 1 | -1,8896 | 0,0388 | -48,70 | 0,000 | 1,50 |
| 4 | -0,2279 | 0,0388 | -5,87 | 0,000 | 1,50 |
| 7 | 0,8854 | 0,0388 | 22,82 | 0,000 | 1,50 |
| Conc*Time | | | | | |
| 2 1 | -0,4413 | 0,0388 | -11,37 | 0,000 | 1,50 |
| 2 4 | 0,2871 | 0,0388 | 7,40 | 0,000 | 1,50 |
| 2 7 | -0,1762 | 0,0388 | -4,54 | 0,000 | 1,50 |

### Regression Equation

D [4;3] = 6,2546 + 1,4429 Conc_2 - 1,4429 Conc_4 - 1,8896 Time_1 - 0,2279 Time_4
+ 0,8854 Time_7 + 1,2321 Time_24 - 0,4413 Conc*Time_2 1 + 0,2871 Conc*Time_2 4

- 0,1762 Conc*Time_2 7 + 0,3304 Conc*Time_2 24 + 0,4413 Conc*Time_4 1
- 0,2871 Conc*Time_4 4 + 0,1762 Conc*Time_4 7 - 0,3304 Conc*Time_4 24

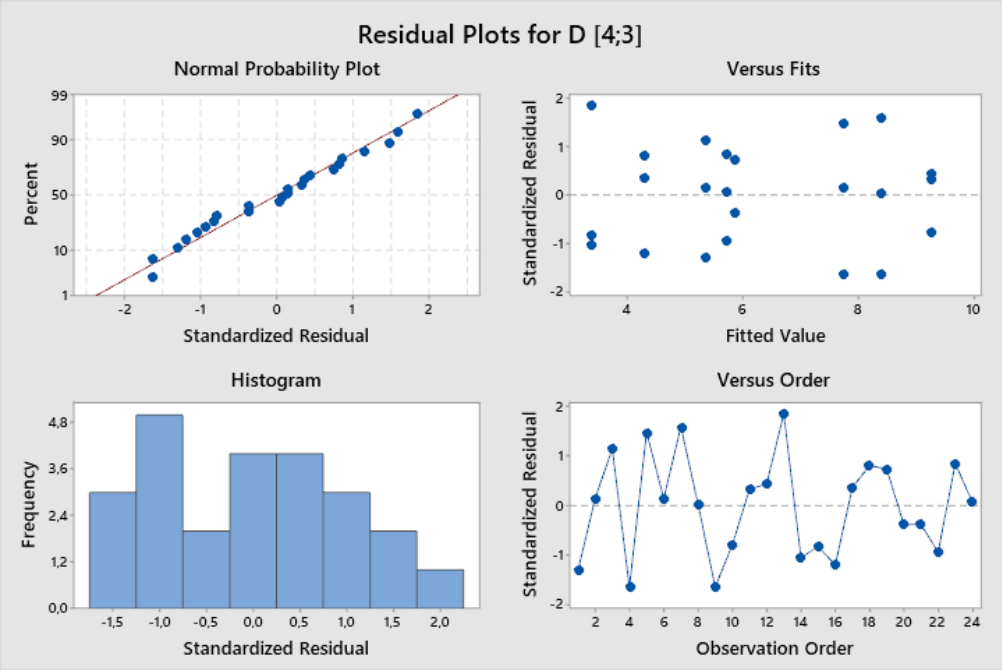


## Comparisons for D [4;3]

### Tukey Pairwise Comparisons: Conc

### Grouping Information Using the Tukey Method and 95% Confidence

| Conc | N | Mean | Grouping | |
|---|---|---|---|---|
| 2 | 12 | 7,69750 | A | |
| 4 | 12 | 4,81167 | | B |

*Means that do not share a letter are significantly different.*

### Tukey Pairwise Comparisons: Time

### Grouping Information Using the Tukey Method and 95% Confidence

| Time | N | Mean | Grouping | | |
|---|---|---|---|---|---|
| 24 | 6 | 7,48667 | A | | |
| 7 | 6 | 7,14000 | | B | |
| 4 | 6 | 6,02667 | | | C |
| 1 | 6 | 4,36500 | | | D |

*Means that do not share a letter are significantly different.*

### Tukey Pairwise Comparisons: Conc*Time

### Grouping Information Using the Tukey Method and 95% Confidence

| Conc*Time | N | Mean | Grouping |
|---|---|---|---|
| 2 24 | 3 | 9,26000 | A |
| 2 7 | 3 | 8,40667 | B |
| 2 4 | 3 | 7,75667 | C |
| 4 7 | 3 | 5,87333 | D |
| 4 24 | 3 | 5,71333 | D |
| 2 1 | 3 | 5,36667 | E |
| 4 4 | 3 | 4,29667 | F |
| 4 1 | 3 | 3,36333 | G |

*Means that do not share a letter are significantly different.*

## C. MATLAB Codes

### C.1 Quantification tool for 2D Spin Echo images

```
Ich % --------------------------------------------------------------------------
% Script Name: Spin Echo 2D Image Multi Interactive Analysis
% Version: 1.0
% Author: Erdem Mercan
% Date: June 20, 2023
% --------------------------------------------------------------------------

%Bu image processor roiPos kısmında olan bir rectangle of interest için
%secilen ana klasördeki tüm alt klasorlerde SpinEcho2Dimageresults.mat file
%ını arar ve her biri için belirlenen analizleri gerçekleştirip seçilen ana
%file içinde bir excel file ına kaydeder.

clc;
clear all;
close all;
% Define ROI position and size
%roiPos = [22 14 23 40];
% Define ROI position and size
roiPos = [23 33 23 18];
% Define ROI position and size
%roiPos = [22 26 23 28];

%roiPos = [22 35 23 17];
% Initialize a cell array to store the results and the subImages
results = {};

% Get the main folder
mainFolder = uigetdir;

% Get the subfolders in the main folder
subFolders = dir(mainFolder);
subFolders = subFolders([subFolders.isdir] & ~strcmp({subFolders.name},'.') &
~strcmp({subFolders.name},'..'));

% Create a new figure before the loop for subImages
figure;

% Process each subfolder
for subFolderIdx = 1:length(subFolders)
    % Get the path to the SpinEcho2Dimageresults.mat file
    matFilePath = fullfile(mainFolder, subFolders(subFolderIdx).name,
'SpinEcho2Dimageresults.mat');
```

```
    % Check if the .mat file exists
    if exist(matFilePath, 'file')
        % Load the .mat file
        matData = load(matFilePath);

        % Check if the 'SeqLoop' variable exists in the loaded data
        if isfield(matData, 'SeqLoop') && isfield(matData.SeqLoop.data, 'Image')
            SEImage = rot90(squeeze(abs(matData.SeqLoop.data.Image)));

            % Extract sub-region from the image
            subImage = SEImage(roiPos(2):(roiPos(2)+roiPos(4)),
roiPos(1):(roiPos(1)+roiPos(3)));

            % Plot the subImage
            subplot(ceil(sqrt(length(subFolders))), ceil(sqrt(length(subFolders))),
subFolderIdx);
            imshow(subImage, []);
            colormap('jet');

            % Get the pixel values within the ROI
            roiPixelValues = subImage(:);

            % Check if there are any valid pixel values within the ROI
            if any(roiPixelValues)
                % Calculate the metrics
                meanRoiIntensity = mean(roiPixelValues(:));
                stdRoiIntensity = std(double(roiPixelValues(:)));
                totalIntensity = sum(roiPixelValues(:));
                minIntensity = min(roiPixelValues(:));
                maxIntensity = max(roiPixelValues(:));
                roiSize = numel(roiPixelValues);
                skewnessIntensity = skewness(double(roiPixelValues(:)));
                kurtosisIntensity = kurtosis(double(roiPixelValues(:)));
                sortedValues = sort(roiPixelValues(:));
                avg5Min = mean(sortedValues(1:10));
                avg5Max = mean(sortedValues(end-9:end));

                % Store the results
                results = [results; {subFolders(subFolderIdx).name,
meanRoiIntensity, stdRoiIntensity, totalIntensity, minIntensity, maxIntensity,
roiSize, skewnessIntensity, kurtosisIntensity, avg5Min, avg5Max}];
            else
                % Store N/A for this subfolder
                results = [results; {subFolders(subFolderIdx).name, 'N/A', 'N/A',
'N/A', 'N/A', 'N/A', 'N/A', 'N/A', 'N/A', 'N/A', 'N/A'}];
            end
        else
            fprintf('The .mat file in subfolder %s does not contain the SeqLoop
variable or its data.Image field.\n', subFolders(subFolderIdx).name);
        end
    else
        fprintf('No .mat file found in subfolder %s.\n',
```

```
subFolders(subFolderIdx).name);
    end
end

% Create a table from the results
resultsTable = cell2table(results, 'VariableNames', {'SubFolder', 'Mean_Intensity',
'Std_Deviation', 'Total_Intensity', 'Min_Intensity', 'Max_Intensity', 'ROI_Size',
'Skewness', 'Kurtosis', 'Avg_5_Min_Intensities', 'Avg_5_Max_Intensities'});

% Display the table
disp(resultsTable);

% Define the name of the excel file
excelFileName = 'resultsimaging.xlsx';

% Define the full file path
fullFilePath = fullfile(mainFolder, excelFileName);

% Write the table to the Excel file
writetable(resultsTable, fullFilePath);
```

## C.2 MATLAB code for $T_1$ and $T_2$ Mapping Analysis

```
clc;
clear all;

% Initialize an empty table
ResultsTable = table({}, [], [], [], [], [], [], {}, 'VariableNames', {'Filename',
'MeanValue', 'TotalValue', 'StdValue', 'AggregationPercentage', 'Contrast',
'Homogeneity', 'VerticalAverages'});

% UI for folder selection
folder_name = uigetdir;

if isequal(folder_name, 0)
    disp('User cancelled folder selection.');
    return;
end

% Get .fig files
fig_files = dir(fullfile(folder_name, '*.fig'));

% Limits for the x-axis of the histogram
minValue = 0.05; % Set minimum limit
maxValue = 0.8; % Set maximum limit
```

```
% Create a cell array to store histograms
histogramData = cell(length(fig_files), 1);

% Process each .fig file
for k = 1:length(fig_files)
    fullpath = fullfile(fig_files(k).folder, fig_files(k).name);

    f = openfig(fullpath, 'new', 'invisible');
    axesObjs = get(f, 'Children');
    dataObjs = get(axesObjs, 'Children');

    imageFound = false;
    for i = 1:length(dataObjs)
        if strcmp(get(dataObjs{i}, 'Type'), 'image')
            cdata = get(dataObjs{i}, 'CData');
            imageFound = true;
            break;
        end
    end

    if not(imageFound)
        disp([fig_files(k).name ' does not contain an image.']);
        continue;
    end

    cdata = flipud(cdata);
    cdata(isnan(cdata)) = 0; % Convert NaN values to 0

    % Determine ROI boundaries based on the dimensions of cdata
    [rows, cols] = size(cdata);
    roi_side_length = min([rows, cols, 48]); % Set ROI side length to be no larger
than half of the smallest dimension or 15
    roi_pos = [max(1, cols/2 - floor(roi_side_length/2)) max(1, rows/2 -
floor(roi_side_length/2)) roi_side_length roi_side_length];
    cdata_roi = cdata(roi_pos(2):(roi_pos(2)+roi_pos(4)-1),
roi_pos(1):(roi_pos(1)+roi_pos(3)-1));

    % Store histogram data
    histogramData{k} = cdata_roi(:);  % Flatten the ROI for histogram plotting

    % Add results to the table
    mean_val = mean(cdata_roi(:));
    total_val = sum(cdata_roi(:));
    std_val = std(cdata_roi(:));
    threshold = 0.165;
    aggregated_percentage = (sum(cdata_roi(:) > threshold) / numel(cdata_roi)) *
100;
    GLCM = graycomatrix(cdata_roi, 'NumLevels', 256, 'Offset', [0 1]);
    texture_props = graycoprops(GLCM, {'contrast', 'homogeneity'});
    vert_avg = mean(cdata_roi, 2);
    VerticalAvgTable = array2table(vert_avg, 'VariableNames', {'VerticalAverage'});
    ResultsTable = [ResultsTable; {fig_files(k).name, mean_val, total_val, std_val,
```

```
aggregated_percentage, texture_props.Contrast, texture_props.Homogeneity,
{VerticalAvgTable}}];

    close(f); % Close the opened figure
end

% Display histograms separately in a 2x2 layout in an extra figure
histFigure = figure;
for j = 1:min(20, length(histogramData))  % Ensure not to exceed the number of
available histograms
    subplot(4, 4, j);
    histogram(histogramData{j}, 50, 'BinLimits', [minValue, maxValue]);
    title(['Histogram: ' fig_files(j).name]);
    xlabel('T2 Values');
    ylabel('Pixel Count');
end

% Display results
disp('Results:');
disp(ResultsTable)
```